Acta Neuropathologica Communications

RESEARCH

Open Access

Dose-dependent CHCHD10 dysregulation dictates motor neuron disease severity and alters creatine metabolism

Sandra Harjuhaahto[1], Manu Jokela[2,3], Jayasimman Rajendran[1], Minea Rokka[1], Bowen Hu[1], Jouni Kvist[1], Fuping Zhang[1,4], Tomáš Zárybnický[1], Kimmo Haimilahti[5], Liliya Euro[1], Eija Pirinen[5,6,7,8], Nadine Huber[9], Sanna-Kaisa Herukka[10,11], Annakaisa Haapasalo[9], Emilia Kuuluvainen[12,13], Swetha Gopalakrishnan[12], Pekka Katajisto[12,13,14], Ville Hietakangas[13], Thibaut Burg[15,16], Ludo Van Den Bosch[15,16], Xiaoping Huang[17], Derek P. Narendra[17], Satu Kuure[1,4], Emil Ylikallio[1,18] and Henna Tyynismaa[1,19,20*]

Abstract

Dominant defects in CHCHD10, a mitochondrial intermembrane space protein, lead to a range of neurological and muscle disease phenotypes including amyotrophic lateral sclerosis. Many patients present with spinal muscular atrophy Jokela type (SMAJ), which is caused by heterozygous p.G66V variant. While most disease variants lead to aggregation of CHCHD10 and activation of proteotoxic stress responses, the pathogenic mechanisms of the p.G66V variant are less clear. Here we report the first homozygous CHCHD10 patient, and show that the variant dosage dictates the severity of the motor neuron disease in SMAJ. We demonstrate that the amount of the mutant CHCHD10 is reduced, but the disease mechanism of p.G66V is not full haploinsufficiency as residual mutant CHCHD10 protein is present even in a homozygous state. Novel knock-in mouse model recapitulates the dose-dependent reduction of mutant CHCHD10 protein and the slow disease progression of SMAJ. With metabolome analysis of patients' primary fibroblasts and patient-specific motor neurons, we show that CHCHD10 p.G66V dysregulates energy metabolism, leading to altered redox balance and energy buffering by creatine metabolism.

Keywords CHCHD10, CHCHD2, ALS, Mitochondria, Creatine, Metabolomics

Introduction

Dominant *CHCHD10* variants cause a spectrum of pathology from muscle to neuronal involvement, with a strong genotype-phenotype correlation. Variants p.S59L and p.R15L are a cause of amyotrophic lateral sclerosis (ALS) and/or frontotemporal dementia (FTD) [1–6], while p.G58R causes mitochondrial myopathy and cardiomyopathy [7]. However, currently the most common pathogenic variant in *CHCHD10*, is heterozygous p.G66V, because of its relatively high allele frequency in Finland [8–10]. It causes spinal muscular atrophy Jokela type (SMAJ, OMIM #615048), originally named late-onset spinal motor neuronopathy (LOSMoN) [9]. SMAJ symptoms typically start around age 40, with muscle cramps, increasing lower limb predominant muscle weakness, hyporeflexia and difficulties in walking. Electromyography (EMG) and muscle biopsies show neurogenic findings such as fiber type grouping, along with secondary myopathic signs such as fatty replacement and

*Correspondence:
Henna Tyynismaa
henna.tyynismaa@helsinki.fi

Full list of author information is available at the end of the article

increased internal nuclei [8, 9]. Serum creatine kinase (CK) is typically elevated in SMAJ, and our previous biomarker analysis of the unique cohort of SMAJ patients' serum samples showed a positive correlation between creatine levels and disease severity [11]. No significant mitochondrial muscle pathology has been detected in SMAJ [12], and accordingly the mitochondrial myopathy markers FGF21 and GDF15 were not increased in patient serum [11]. The disease mechanism of SMAJ, and how it differs from the other CHCHD10-linked phenotypes, is not known.

CHCHD10 is a small mitochondrial protein of unknown function, localizing to the intermembrane space (IMS). It can form complexes with its homologue protein CHCHD2 and is frequently found in complexes of 170 to 220 kDa [13, 14]. CHCHD10 is likely to interact with other proteins in IMS and mitochondrial inner membrane (IMM), possibly providing stability or facilitating interactions. Surprisingly CHCHD2/CHCHD10 are largely dispensable in human cell and animal models. Although the expression of CHCHD2/CHCHD10 aligns with oxidative phosphorylation (OXPHOS) complex expression and is induced by OXPHOS defects [10], the loss of CHCHD2/CHCHD10 has had only mild effects on mitochondrial respiration in most models. Furthermore, the CHCHD2/CHCHD10 double knockout mouse had a normal life span, although the mouse hearts did show activation of the mitochondrial integrated stress response (mtISR) [15]. CHCHD2/CHCHD10 may thus contribute to the regulation of OXPHOS function and mitochondrial homeostasis in a temporal and cell-specific manner, with relevance for human neuropathologies.

Several comprehensive studies have identified a toxic gain-of-function mechanism for the p.S59L and p.G58R variants, marked by aggregated CHCHD10 and CHCHD2 [16–20]. CHCHD10 protein has regions that are intrinsically disordered, which may drive its aggregation [10]. Both p.S59L and p.G58R knock-in mouse models developed a fatal cardiomyopathy [16, 17, 20]. The mice presented with activated mtISR via OMA1-dependent cleavage of DELE1 in the heart [20]. Cleaved DELE1 is transported into cytosol where it activates the HRI kinase, which in turn phosphorylates eIF2a, leading to attenuation of global protein translation and increased expression of specific transcripts, such as *ATF4*, *ATF5*, and *CHOP* [21]. Subsequently to mtISR activation, the p.S59L and p.G58R knock-in mice exhibited extensive metabolic rewiring, enhancement of transsulfuration and one carbon metabolism, and antioxidant responses leading to heme depletion [19].

On the contrary, haploinsufficiency has been suggested as a mechanism for the p.G66V variant, as approximately 50% reduction of CHCHD10 protein was detected in p.G66V patient cells [22]. The p.G66V variant has been proposed to alter the structure and intramolecular interactions of the CHCHD10 protein, affecting its stability and increasing its susceptibility to degradation [23, 22]. Given the slow progression of SMAJ, reduced CHCHD10 availability could be a factor influencing mitochondrial homeostasis, and playing a direct role in disease pathogenesis. Perhaps specific cell types could be more susceptible to lowered CHCHD10 amount, explaining why the tissue involvement is limited to the neuromuscular system in SMAJ. Indeed, in spinal motor neurons differentiated from human pluripotent stem cells (iPSC) the loss of CHCHD10 caused increased proton leakage and reduced spare respiration capacity [24]. Furthermore, one study of CHCHD10 knockout mice has reported neuromuscular junction impairment [25]. However, human variation data suggest that CHCHD10 loss-of-function variants are well-tolerated [10], arguing against pure haploinsufficiency as the mechanism of the heterozygous p.G66V variant. Therefore, defining the exact pathogenic mechanism of the p.G66V variant requires further investigations.

Here we describe the phenotype of the first patient with a homozygous pathogenic variant in *CHCHD10*, and evaluate whether haploinsufficiency is a valid mechanism for the p.G66V variant. We examined patients' skin fibroblasts, as well as motor neurons differentiated from patient-specific and genome-edited iPSC, and a novel p.G66V knock-in mouse model. First, we found that the homozygous p.G66V variant causes a more severe disease phenotype resembling mitochondrial myopathy compared to the heterozygous variant. Second, we observed dose-dependent reduction of the CHCHD10 protein in in vitro and in vivo. Third, contrary to other *CHCHD10* variants, p.G66V variant did not lead to proteotoxic aggregation of mutant CHCHD10, and mtISR activation was observed solely in patient fibroblasts. Finally, we propose that rewiring of creatine metabolism is part of SMAJ pathogenesis.

Materials and methods

Homozygous patient clinical assessment

The patient underwent a thorough neurological evaluation by an experienced neurologist (MJ). Muscle imaging, EMG/NCS and muscle biopsy evaluation were performed for diagnostic purposes according to standard methods. Muscle MRI was conducted using routine T1-weighted sequences of lower limb muscles. Mitochondrial DNA deletions were investigated by XL-PCR. The amplification reactions were carried out by using Phusion High-Fidelity DNA Polymerase (Thermo Fisher Scientific, Waltham, MA, U.S.A.) with GC buffer for long templates using primers (supplemental Table 2) according to the provided protocol.

Fibroblast cell culture

Human fibroblast cultures were established from skin punch biopsies and cultured by standard methods. Briefly, cells were cultured in at 37℃, in a humidified atmosphere, normoxia and 5% CO_2. Fibroblasts were maintained in DMEM media (Lonza #12–614 F) supplemented with 2mM L-Glutamate (Life Technologies #250300081), 10% FBS (Life Technologies #10270106), 1x penicillin/streptomycin (Life Technologies #15140122) and 50 µg/mL Uridine (Sigma #U3003). Fibroblasts of one homozygous and one heterozygous patient and three to four healthy volunteer controls were used for the experiments.

iPSC cell culture

IPSC were maintained on Matrigel-coated (Corning) plates with DMEM/F12 with GlutaMAX medium (Gibco) supplemented with ESSENTIAL 8-supplement (Gibco). Cells were cultured at 37 °C in 5% CO2, 20% O2. IPSC were maintained on Matrigel-coated (Corning) plates in Essential 8 (E8) medium (Gibco) supplemented with Primocin (100 µg/ml) (Invivogen). IPSC were passaged using 0.5 mM EDTA (Invitrogen) in phosphate-buffer saline (PBS) when confluent.

Genome editing of iPSC

CRISPR-*Sp*Cas9 technology was used to correct heterozygous p.G66V variant and create isogenic control iPSC line upon homology-directed repair. The crRNA sequences were designed using online analysis tools Crispor version 4.97 (Concordet & Haeussler, 2018; http://crispor.tefor.net/), Benchling (https://benchling.com/crispr) and IDT CRISPR/ Cas9 design checker (https://www.idtdna.com/). The ribonucleoprotein (RNP) components (HiFi Cas9 protein, crRNA and tracrRNA) were purchased from Integrated DNA Technologies (IDT) and prepared based on the manufacturer's protocol. The guide RNA together with Cas9 in a complexed (RNP) was delivered by electroporation using the Neon Transfection System (ThermoFisher) to 2 million TrypLE Select (Thermo Scientific) dissociated heterozygous patient cells, together with 4 µM electroporation enhancer (IDT), and 2 µM of ssODN donor template (IDT). Electroporated samples were plated immediately onto pre-warmed 35 mm cell culture plates supplemented with RevitaCell (Thermo Scientific) and 10 µM Alt-R HDR enhancer (IDT). Limited dilution cloning for electroporated iPSC pool was done according to Bruntatraeger et al. Briefly, 500–1000 TrypLE Select dissociated cells were plated into 10 cm tissue-culture dishes coated with Vitronectin XF (STEMCELL Technologies) at a concentration of 5 µg/cm2 containing 10 mL with TeSR™-E8™ (STEMCELL Technologies) media supplemented with 1X CloneR (STEMCELL Technologies). 48 h after subcloning, cell culture medium was replaced with 10 mL of Essential 8 Flex medium supplemented with E8 Flex medium supplement (Gibco) and changed every 48 h for 8 days until colony picking. Recombinant colonies were validated using Sanger sequencing and checked for chromosomal abnormalities by G-banding karyotyping. Off-target genome editing was evaluated with CRISPOR Batch Gene Targeting Assistant 4.97. Regions with highest cutting frequency determination (CFD) score were analysed using Sanger sequencing.

Motor neuron differentiation

To differentiate iPSCs into motor neurons, we used the protocol by [26] with slight modifications. Briefly, to obtain neuroepithelial stem cells, iPSCs were dissociated with Accutase (Gibco) into small clusters and resuspended in E8 medium containing 5 µM Y-27,632 (Selleckchem). The following day, medium was changed to Neuronal basal medium (DMEM F12, Neurobasal vol: vol, with N2 (Life Technologies), B27 (Life technologies) and l-ascorbic acid 0.1 mM (Santa Cruz)) supplemented with 40 µM SB431542 (Merck), 0.2 µM LDN-193,189 (Merck/Sigma), 3 µM CHIR99021 (Selleckchem), and 5 µM Y-27,632 (Selleckchem). From day 3 on, 0.1 µM retinoic acid (Fisher) and 0.5 µM SAG (Calbiochem) was added to neurobasal medium. From day 7 on, BDNF (10 ng/ml, Peprotech) and GDNF (10 ng/ml, Peprotech) were added. 20 µM DAPT (Calbiochem) was added on day 9. Motor neuron progenitor spheroids were dissociated into single cells for plating on day 11 by using Accumax (Invitrogen). Motor neuron progenitors were subsequently plated on poly-d-lysine 50 µg/ml (Merck Millipore) and laminin 10 µg/ml (Sigma-Aldrich) coated plates at 5×10^4 cells per cm2. At day 14 retinoic acid and SAG were removed from media. From day 16 on, the cells were switched to motor neuron maturation medium supplemented with BDNF, GDNF, and CNTF (each 10 ng/ml, Peprotech). Media were changed every other day by replacing half of the medium. Motor neurons were HB9-positive around day 30 of differentiation, after which they were considered mature.

Mouse maintenance

Animal experiments were performed in compliance with the national ethical guidelines set by the European Union and were approved by the National Animal Experiment Board (Project Authorisation Board). The ethical practice of handling laboratory animals was strictly followed throughout the procedures. The mice were housed at 22 °C with 12-hour light/dark cycles with *ad libitum* access to standard rodent food and water. Mice weight development was measured every 10 days beginning at P150 until end point.

Chchd10^{G66V} mouse generation and genotyping

Novel heterozygous and homozygous Chchd10 p.G66V (c.186G>T, p.G62V in mouse genome) knocking mice were generated with CRISPR/Cas9 editing as part of the FinnDisMice project, where novel mouse models were generated to analyze group of hereditary monogenic disorders found enriched in Finnish population [27]. In brief, the combination of gRNA gRNA1: TCAGCTGTAG GGCATGTCATGGG and a ssDNA repair template were employed to introduce the human 194G>T(66G/V) variant in C57BL/6J (Janvier Labs) mouse corresponding the nucleotide change at 186G>T, (62G/V).

The genotyping of founders and actual mouse cohort was carried out by PCR from ear marks. The DNA was extracted using the Extracta DNA Prep for PCR (95091-025, Quantabio) and used as a template for the PCR reaction, amplified by DreamTaq DNA Polymerase (EP0705, Thermo Fisher) using the SimpliAmp™ Thermal Cycler (A24811, Thermo Fisher). The genomic region of interest was amplified by primer pair of sense: GCCTCCTGCGC ACCCACCAC and antisense: CCTCCGTTTCTTGAGT CCTC. Enzyme digestion of the 224 bp PCR product by BaeGI (NEB) had been used for the Gle1 KI mice to distinguish the carriers of the insertion.

Sex as a biological variable

Our study examined male and female animals, and similar findings are reported for both sexes.

Metabolomics (fibroblasts, iPSC, d14 MN, d35 MN, mouse muscle, and mouse serum)

Metabolites were extracted with ice cold Acetonitrile: H2O (80:20) extraction solvent. 20 mg muscle tissue, 50 uL serum, and confluent 3,5 cm plates cell cultures were used for metabolite extraction. Samples were centrifuged 13 000 rpm, 10 min at +4 °C and the supernatant was stored in -80 °C until further processing. Samples were analyzed on a Thermo Q Exactive Focus Quadrupole Orbitrap mass spectrometer coupled with a Thermo Dionex UltiMate 3000 HPLC system (Thermo Fisher Scientific). The HPLC was equipped with a hydrophilic ZIC-pHILIC column (150 × 2.1 mm, 5 µm) with a ZIC-pHILIC guard column (20 × 2.1 mm, 5 µm, Merck Sequant). A total of 5 µl sample was injected into the LC–MS instrument after quality controls in randomized order having every tenth samples as blank. A linear solvent gradient was applied in decreasing organic solvent (80–35%, 16 min) at 0.15 ml min−1 flow rate and 45 ∘C column oven temperature. Mobile phases were aqueous 200 mmol per litre ammonium bicarbonate solution (pH 9.3, adjusted with 25% ammonium hydroxide), 100% acetonitrile and 100% water. Ammonium bicarbonate solution was kept at 10% throughout the run, resulting in a steady 20 mmol per litre concentration. Metabolites were analysed using a mass spectrometer with a heated electrospray ionization source using polarity switching and the following settings: resolution of 70,000 at m/z of 200; spray voltages of 3400 V for positive and 3000 V for negative mode; sheath gas of 28 arbitrary units (AU) and auxiliary gas of 8 AU; vaporizer temperature of 280 ∘C; and ion transfer tube temperature of 300 ∘C. The instrument was controlled using Xcalibur 4.1.31.9 software (Thermo Scientific). Metabolite peaks were confirmed using commercial standards (Sigma Aldrich). Data quality was monitored throughout the run using an inhouse quality control cell line extracted in a similar manner to other samples. After final peak integration with TraceFinder 4.1 SP2 software (Thermo Scientific), peak area data were exported as Excel files. Missing values were replaced with zeros, while flagging the number of missing metabolites. Metabolite peak areas were log1p-transformed and quantile normalized using voom [28]. The differential expression between genotypes was analysed in R (R Core Team, 2021) with limma [28] using lmFit with eBayes correction on the contrasts between genotypes (and depending on the experiment also other factors such as developmental stage, sex and tissue). Metabolites with FDR-corrected p-values < 0.05 were considered differentially expressed, if they contained less than 2 missing values. Enrichment analysis on DE metabolites were performed using metaboanalyset V6.0 (https://www.metaboanalyst.ca). PCA was calculated using prcomp (R Core Team, 2021). Figures were generated with ggplot2 [29].

Proteomics (d14 MN)

Neuronal media was removed form d14 MN motor neuron cultures. Cells were pelleted and then lysed with 50 uL of 6 M Urea 50 nM Tris-HCl buffer. Proteomics analysis was done in Biocenter of Turku. Protein identifications was done using DirectDIA and label free quantifications was done with MaxLFQ using Spectronaut software (Biognosys; version 18.0.2) against Swiss-Prot (2023_01 Homo Sapiens) and Universal Protein Contaminant database [30]. Precursor and protein detection FDR cutoff was 0.05. Quantification was carried out at MS2 level with area under the curve within integration boundaries for each targeted ion. The protein peak areas were exported from Spectronaut and analysed in R with limma [28] the same ways as the metabolomics data.

RNAseq (mouse muscle)

Total RNA was extracted from 20 mg mouse skeletal muscle using TRIsure-chloroform-ethanol (Bioline) method followed by in-column DNA digestion (Qiagen). RNA quality determination and mRNA sequencing were done at Biomedicum Functional Genomics Unit at the Helsinki Institute of Life Science and Biocenter Finland at the University of Helsinki with single-end sequencing

with poly (A) binding beads and NEBNext Ultra II Directional RNA Library Prep and sequenced with Illumina NextSeq High Output 1 × 75 bp. Raw data (bcl-files) was demultiplexed with bcl2fastq2 (Illumina). The fastq-files were filtered with cutadapt [31] to remove adapter sequences, ambiquous (N) and low quality bases (Phred score < 25). Reads that were too short (< 25 bp) after trimming were excluded. The filtered fastq-files were mapped to the mouse reference genome (GENCODE-GRCm39) with STAR [32]. The mapped reads were analyzed with R (R Core Team, 2021). Read counts for genes were extracted with Rsubreads [33] excluding duplicates, multimapping reads, chimeric fragments, and reads with mapping quality below 10. Differential gene expression was analyzed with DESeq2 [34], comparing the genotypes to each other. Genes with low reads depth (< 50 reads in total) were excluded. Genes with FDR corrected *p*-value < 0.01 were considered differentially expressed. PCA, and figures were done the same way as with the proteomics and metabolomics datasets.

Statistical analysis

GraphPad Prism 10 was used for all statistical analyses except transcriptomics, proteomics and metabolomics. One-way ANOVA was used for the experiments with post-hoc Fisher's LSD test to determine statistical differences between groups (comparisons always between heterozygous vs. its isogenic control (WT_isogenic), and homozygous vs. WT), mean ± SD values are reported in the graphs. $P < 0.05$ were considered significant. All measured data points were included in the analysis. Values for all data points in graphs are reported in the Supporting Data Values file.

Additional information about materials and methods used in this study is provided as supplemental material.

Results

Phenotype of the individual carrying a biallelic CHCHD10 p.G66V variant

The individual with homozygous c.197G > T p.G66V variant is a son of father and mother from two previously reported SMAJ pedigrees (Fig. 1A). He was first examined at 3 years of age because of walking difficulties and stumbling and was noted to have absent tendon reflexes and tight heel cords, which were later surgically corrected. Due to the patient's young age, only a limited EMG/nerve conduction study was performed at the time, and it showed neurogenic, predominantly motor abnormalities. In childhood, the patient was clumsy but could participate in sports, such as running and skating. After age 30, he required a cane for walking and at age 37 was wheelchair-bound but able to stand for short periods of time. Severe lower limb and moderate upper limb weakness and atrophy was present, in addition to bulbar and respiratory muscle weakness (Fig. 1B). Vibration sensation was absent in all limbs. Despite tongue atrophy (Fig. 1B), the patient had normal speech and was able to work in a cognitively demanding job. Brain MRI was normal. CK was 2-fold elevated and muscle MRI showed subtotal fatty replacement of lower limb muscles, with moderate involvement in upper limbs and trunk muscles (Fig. 1C). Cardiac ultrasound was normal. Muscle biopsy showed mitochondrial pathology with 15–20% COX-negative and SDH hyperreactive fibers, ragged red fibers with fiber size variability and internalized nuclei in 80% of muscle fibers (Fig. 1D). Electron microscopy (EM) showed defective mitochondria with severely disorganized cristae (Fig. 1E). XL-PCR analysis revealed multiple mitochondrial DNA (mtDNA) deletions in muscle tissue (Fig. 1F). In brief, the patient's condition was consistent with motor neuronopathy leading to proximal and distal muscle wasting, which is more severe than in SMAJ, in addition to sensory impairment and mitochondrial myopathy.

p.G66V variant causes a dose-dependent reduction in CHCHD10 amount and leads to mtISR marker induction in homozygous patient fibroblasts

We obtained skin fibroblasts from the individual with homozygous p.G66V variant as well as from a heterozygous individual and healthy controls. Immunoblotting with CHCHD10 antibody showed reduced CHCHD10 protein in the fibroblasts from both patients (30% reduction in heterozygous and 60% in homozygous patient fibroblasts compared to control average) (Fig. 2A, B). The mRNA expression of *CHCHD10* or *CHCHD2* was not altered (Fig. 2C, supplemental Fig. 1A). Mitochondrial DNA copy number was normal (supplemental Fig. 1B). These findings show that the p.G66V variant reduces the availability of CHCHD10 in a dose-dependent manner in patient cells, but does not lead to its complete absence in homozygous state.

Immunocytochemistry with an antibody against the mitochondrial marker SDHA showed a normal mitochondrial network in fibroblasts from both patients (Fig. 2D). However, the signal for CHCHD10 was reduced in patients' cells in comparison to control cells (Fig. 2D), appearing as punctate signal especially in the homozygous patient cells. These findings prompted us to investigate whether the mtISR was activated in patient fibroblasts similarly as previously reported with other pathogenic variants of *CHCHD10* [16, 17, 19, 20]. Indeed, patient fibroblasts had increased expression of transcripts associated with the mtISR (*ATF4*, *ATF5*, *CHOP10*, *MTHFD2* and *GDF15*) in comparison to control cells (Fig. 2E). The increase was more pronounced in the homozygous patient cells. Notably, the expression of *ATF5* was increased 12.5-fold in the homozygous cells,

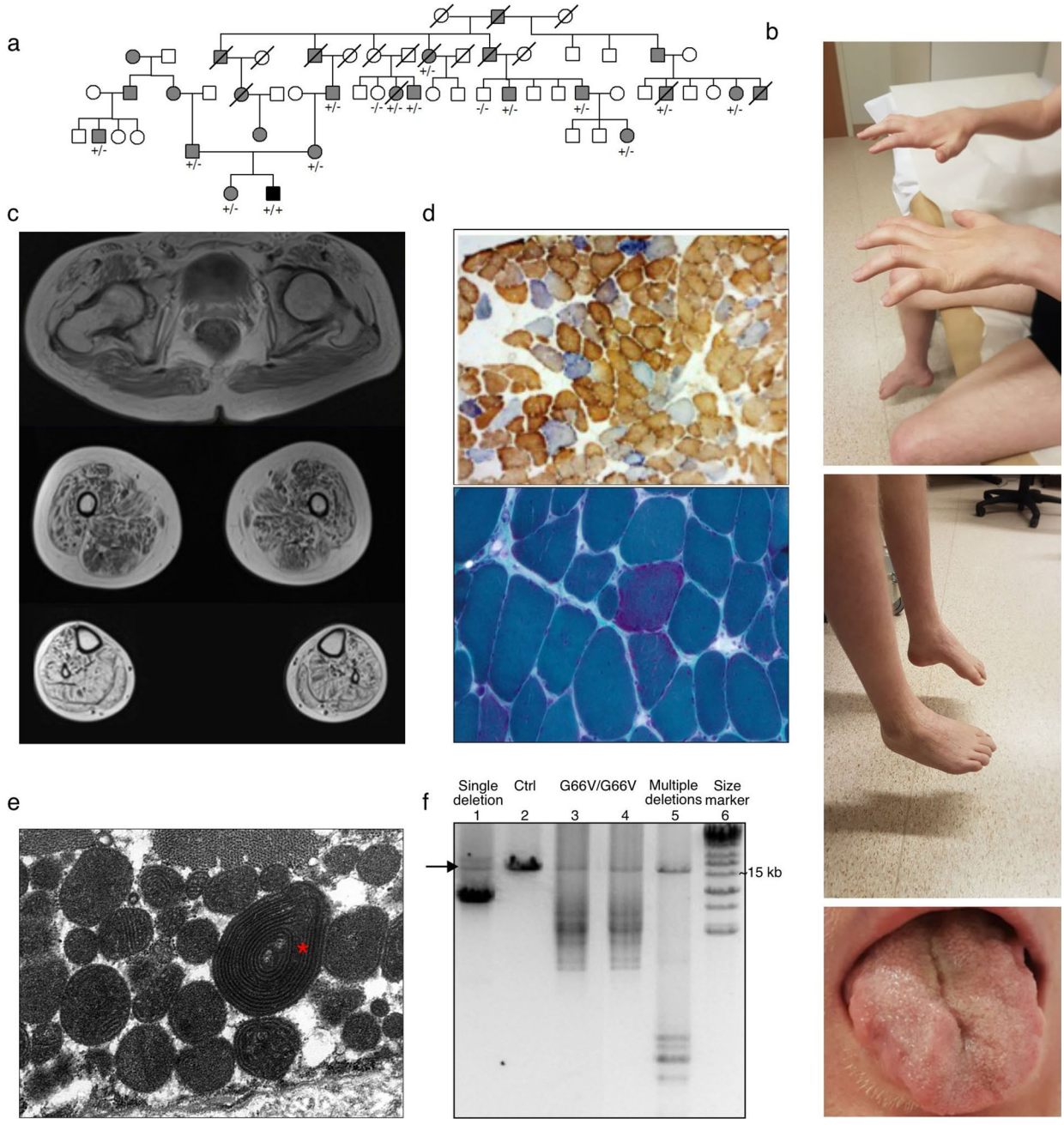

Fig. 1 Phenotype of the unique patient with biallelic *CHCHD10* p.G66V variant. (**A**) Family tree of the investigated patient. Black square indicates the proband. (**B**) Clinical assessment of the proband showed moderate upper limb weakness and severe lower limb atrophy, also in tongue. Metacarpophalangeal hyperextension and the distal and proximal interphalangeal joint flexion caused by weakness of small intrinsic hand muscles (claw hand) (upper panel). Distal lower limb weakness, patient is trying to dorsiflex ankles (middle panel). Weak, atrophic tongue (lower panel). (**C**) MRI showing significant muscle atrophy and fatty tissue replacement of lower limb muscles. (**D**) Mitochondrial pathology with 15–20% COX-negative-SDH hyperreactive fibers, ragged red fibers (Gomori Trichorme) with fiber size variability and internalized nuclei in 80% of muscle fibers. (**E**) Transmission electron micrograph from patient muscle biopsy showing severely disorganized cristae (indicated by red asterisk). (**F**) XL-PCR revealed multiple deletions in mtDNA of the skeletal muscle in the patient with homozygous p.G66V mutation in *CHCHD10*. Lane 1: positive control for single mtDNA deletion from an unrelated patient's muscle biopsy; lane 2: a control subject with no deletions in mtDNA in skeletal muscle; lanes 3 and 4, replicates of the muscle biopsy with homozygous p.G66V variant in *CHCHD10*; lane 5, positive control for multiple mtDNA deletions from an unrelated patient's muscle biopsy; lane 6, size marker. Black arrow indicates the size of intact mtDNA. Black arrow indicates the size of intact mtDNA

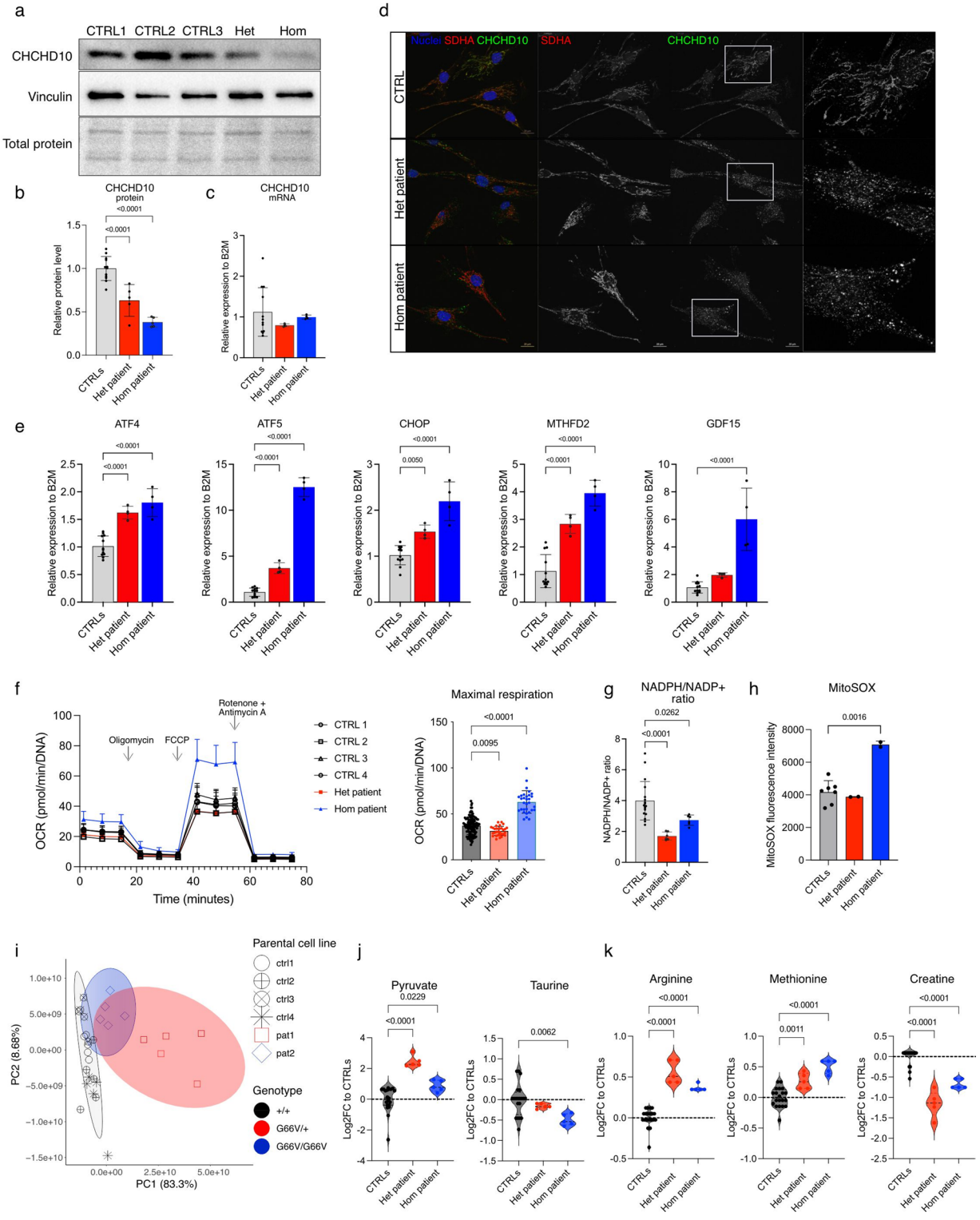

Fig. 2 (See legend on next page.)

compared to 5-fold increase in the heterozygous patient cells, and the expression of *GDF15* was only increased in the homozygous patient cells (6-fold). Despite the upregulation of mtISR marker transcripts, we did not detect an induction of OMA1-dependent OPA1 cleavage in the patient cells, and it was comparable to control cells even when the cells were stressed with actinonin [35] (supplemental Fig. 1C, D). These findings showed that the

(See figure on previous page.)

Fig. 2 Dose dependent changes in expression of integrated stress response markers and one-carbon metabolism in *CHCHD10* p.G66V patient fibroblasts. (**A**) Immunoblot of CHCHD10 levels from whole cell lysates. (**B**) Quantification of CHCHD10 levels from whole cell lysates normalized to total protein (4 control cell lines, $n=3$ technical replicates/ctrl, $n=5$ technical replicates/patient). (**C**) Expression of *CHCHD10* in patient fibroblasts relative to *B2M* (3 control lines, $n=4$ technical replicates each). (**D**) Representative immunocytochemistry images of control and heterozygous and homozygous patient fibroblasts stained with antibody against CHCHD10 (green), SDHA (red) and nucleus (blue). Scale bar 20 µm. (**E**) Expression of *ATF4*, *ATF5*, *CHOP*, *MTHFD2* and *GDF15* in patient fibroblasts relative to *B2M* (3 control lines pooled, $n=4$ technical replicates). (**F**) Oxygen consumption rate (OCR) measurement in fibroblasts using Seahorse XF96 Analyzer. Maximal respiration was assessed following mitochondrial uncoupling by FCCP. 4 ctrl lines pooled, 13–16 technical replicates/cell line/run. All data points shown. Two independent experiments. (**G**) Ratio NADPH/ NADP + was measured with colorimetric assay. Results normalized to total protein amount (3 ctrl lines pooled, 6 technical replicates each). (**H**) Mitochondrial superoxide production measured with MitoSOX assay as fluorescence intensity 4 ctrl lines pooled, 2 technical replicates/cell line). (**I**) PCA plot describing overall variance within metabolite profiles. 4 control cell lines, 5 technical replicates/cell line. (**J**) Increased pyruvate and decreased taurine metabolite levels determined from metabolomics data. 4 control cell lines, 5 technical replicates/cell line (represented as log2(fold change) [log2(FC)]). (**K**) Increased arginine and methionine metabolite levels and decreased creatine in patient fibroblasts determined from metabolomics data. 4 control cell lines, 5 technical replicates/cell line (represented as log2(fold change) [log2(FC)]). Data shown as mean ± standard deviation; $P<0.05$ were considered significant by one-way ANOVA followed by Fisher's LSD's multiple comparison post-hoc test. Quantifications show all measured data points, results are presented relative to the average of all measured control data points

p.G66V variant can induce mtISR marker expression in skin fibroblasts.

Multi-omics study by Straub et al. (2021) reported that patient fibroblasts carrying the *CHCHD10* p.R15L variant had rewiring of one carbon metabolism in association with upregulated proteotoxic stress responses [36]. Therefore, we assessed the metabolic consequences of the p.G66V variant in patient fibroblasts using the Seahorse Extracellular Flux Analyzer, a colorimetric assay for nicotinamide adenine dinucleotides, and targeted metabolomics. The heterozygous patient fibroblasts displayed modestly reduced maximal respiration after FCCP injection. Of note, we also observed slightly reduced maximal respiration and increased expression of mtISR transcripts in the heterozygous patient's primary myoblasts (supplemental Fig. 2A-C). In contrast, homozygous patient fibroblasts showed increased maximal respiration (Fig. 2F and supplemental Fig. 1E). Hypermetabolic phenotypes with increased respiration have been associated with the activation of mtISR, however, mtISR inhibitor treatment with ISRIB did not affect respiration in the homozygous patient fibroblasts (supplemental Fig. 1G-H) [37, 38]. Moreover, both patient fibroblasts displayed decreased NADPH/NADP + ratio (Fig. 2G and supplemental Fig. 1F). Interestingly, homozygous patient fibroblasts showed significantly increased mitochondrial superoxide levels measured as MitoSOX intensity (Fig. 2H). These results support altered redox balance in patient fibroblasts. Targeted metabolite profiling also displayed a marked difference in the metabolism of the patient fibroblasts compared to controls (Fig. 2I). Patient cell lines showed similar changes in the metabolites that we previously detected altered in serum samples of the heterozygous SMAJ patients [11]. Both in serum and in the fibroblasts, pyruvate was increased and taurine decreased (Fig. 2J). Moreover, creatine was decreased in the patient fibroblasts, and its precursors, arginine and methionine, were increased (Fig. 2K), supporting the altered creatine metabolism in SMAJ pathogenesis.

In summary, homozygous p.G66V causes a larger reduction in CHCHD10 protein amount in fibroblasts than the heterozygous variant, leading to a higher induction of *ATF5* and *GDF15* expression as markers of mtISR, suggesting a similar response as has been observed with other CHCHD10 pathogenic variants. On the other hand, heterozygous patient fibroblasts showed only modestly increased mtISR markers. However, changes in redox balance and creatine metabolism were present in both patient lines.

mtISR marker induction is diminished upon differentiation of patient iPSC into spinal motor neurons

Next, we investigated the effects of the p.G66V in a disease-relevant human cell type, motor neurons. We reprogrammed the heterozygous and homozygous patient fibroblasts into iPSC, and also generated an isogenic control for the heterozygous patient line by correcting the disease variant via CRISPR/Cas9 gene editing (Fig. 3A, supplemental Fig. 3A). We differentiated the iPSC into motor neurons (MN) using a published differentiation protocol [26] with slight modifications, which we have extensively used in disease modeling [24, 39, 40] (Fig. 3B, supplemental Fig. 3B). We analyzed the iPSC-MN at two different timepoints, on day 14 when motor neurons are post-mitotic (d14-MN) and at day 35 when they have matured (d35-MN). Patient and gene-edited iPSC lines differentiated similarly into HB9-positive MN (Fig. 3C, D). Interestingly, despite normal looking neurite network, the culture media of d35-MN of the homozygous patient contained more neurofilament light (NfL) (Fig. 3E), which is released to culture media in axonal injury [41]. Patient-specific MN had reduced CHCHD10 protein levels (50% reduction in heterozygous d35-MN, 70% reduction in homozygous d35-MN) by immunoblotting, showing dose-dependency similarly to patient fibroblasts (Fig. 3G, H). However, in d14-MN the CHCHD10 protein level reduction was less evident (no reduction in heterozygous and 40% reduction in homozygous

d14-MN), suggesting cell-stage dependent regulation of the stability of the CHCHD10 mutant protein. Immunocytochemistry showed reduced and punctate CHCHD10 signal in d35-MN neurites (Fig. 3F). Similarly to patient fibroblasts, p.G66V variant did not consistently affect *CHCHD10* mRNA expression in iPSC-MN (Fig. 3I).

CHCHD10 is suggested to be involved in mitochondrial cristae organization [1, 14, 42], and altered cristae structure has been previously reported in some models with other *CHCHD10* disease variants. Therefore, we studied the mitochondrial ultrastructure in patient-derived d35-MN with EM (Fig. 3J). Quantification of mitochondrial size from the EM images showed that the heterozygous and homozygous patient MN had smaller mitochondria when compared to those of a healthy control, however, mitochondrial ultrastructure was overall normal (Fig. 3J-K) and mitochondrial DNA copy number was not changed (Fig. 3L). Next, we measured mitochondrial respiration with Seahorse analyzer in d35-MN (Fig. 3M and supplemental Fig. 3C). Homozygous patient MN showed moderately increased maximal respiration similarly to homozygous patient fibroblasts (Fig. 3M), whereas heterozygous MN displayed no significant changes in contrast to fibroblasts.

Unlike the patient fibroblasts, heterozygous d14 or d35-MN did not show a clear induction of mtISR marker expression as determined by quantification of *ATF4*, *ATF5*, *CHOP10* and *MTHFD2* mRNA levels (Fig. 3N), whereas the homozygous patient d35-MN exhibited modestly increased expression of *ATF4* and *CHOP10* at d35-MN. The expression of *MTHFD2* was somewhat increased in patient MN (Fig. 3N), potentially indicating minor changes in one carbon metabolism [19, 36]. The *ATF5* induction that we observed in homozygous patient fibroblasts was maintained in the iPSC reprogrammed from those fibroblasts, but no longer in the MN differentiated from the same iPSC (Fig. 3O). To investigate if it is possible to induce *ATF5* expression as a mtISR marker in cultured MN, we treated control cells with actinonin, and measured *ATF5* expression during differentiation. We observed a striking 50-fold induction of *ATF5* expression in iPSC, but no induction in d35-MN (Fig. 3P). ATF5 has been suggested to block the differentiation of neuroprogenitor cells into neurons and must be downregulated to permit neuronal maturation [43], which could explain why MN could not induce its expression. Our results show that the degree of mtISR induction as a consequence of CHCHD10 p.G66V variant depends on the cell type and its transcriptional program, and has a limited presence in motor neurons. This raises an interesting question of whether mtISR is protective for some cell types, given the limited tissue involvement in SMAJ.

Upregulated creatine metabolism in patient-derived motor neurons

Next, we analyzed metabolic changes during MN differentiation. We performed targeted metabolite profiling for iPSC (d0), d14-MN and d35-MN (Fig. 4A, supplemental Fig. 4A). Interestingly, principal component analysis revealed substantial changes in d14-MN, where heterozygous and homozygous MN clustered separately from the healthy control (WT) and the corrected isogenic heterozygous patient line (WT_isogenic) (Fig. 4A). We decided to focus our analysis on d14-MN data, as for the iPSC and d35-MN metabolite profiles of the patient and control cell lines exhibited less clear separation (supplemental Fig. 4A, enrichment analysis in supplemental Fig. 4B). We also performed a proteome analysis on d14-MN samples (Fig. 4B, supplemental Fig. 4C). This is a particularly important time point for the maturation of mitochondrial respiratory chain, in order to fulfill the demands of oxidative metabolism in mature motor neurons (Torregrosa-Muñumer et al. unpublished observations, manuscript in preparation).

In d14-MN, we observed changes in the same metabolic pathways as in patient fibroblasts and serum. For example, pyruvate level was decreased in heterozygous and homozygous d14-MN, and alanine and malate were increased (Fig. 4C). The GSH/GSSG ratio was increased (Fig. 4D), and levels of several amino acids were changed (Fig. 4E). Creatine metabolism and the urea cycle were altered, based on both the metabolomic and proteomic analysis (Fig. 4F). Namely, the protein level of carbamoyl phosphate synthetase (CPS1) the first and rate-limiting enzyme of urea cycle, was decreased, whereas N-acetylglutamate, which is its obligatory allosteric activator, was increased. CPS1 catalyzes the synthesis of carbamoyl phosphate from glutamate or ammonia. We noted that *CPS1* expression was also downregulated in the dataset of CHCHD10 loss-of-function variant p.R15L fibroblasts upon stress (supplemental Fig. 5A, data from [36]). Moreover, metabolites downstream of CPS1 - ornithine, arginine, methionine, and guanidinoacetate - were decreased. Protein level of guanidinoacetate N-methyltransferase (GAMT), which converts guanidinoacetate to creatine, was increased, as well as creatine. In addition, the protein level of plasma membrane transporter of creatine SLC6A8 was increased (Fig. 4F). Reduction of precursors and increased end-product suggest elevated creatine production rate. These results indicate rewiring of creatine metabolism in maturing MN with p.G66V mutant CHCHD10, also proposing a window in neuronal development where CHCHD10 function may be critical.

Next, we analyzed in more detail the proteome changes in patient-derived d14-MN. We observed that many subunits and assembly factors of the OXPHOS complex IV (COX) were increased (Fig. 4G), whereas other

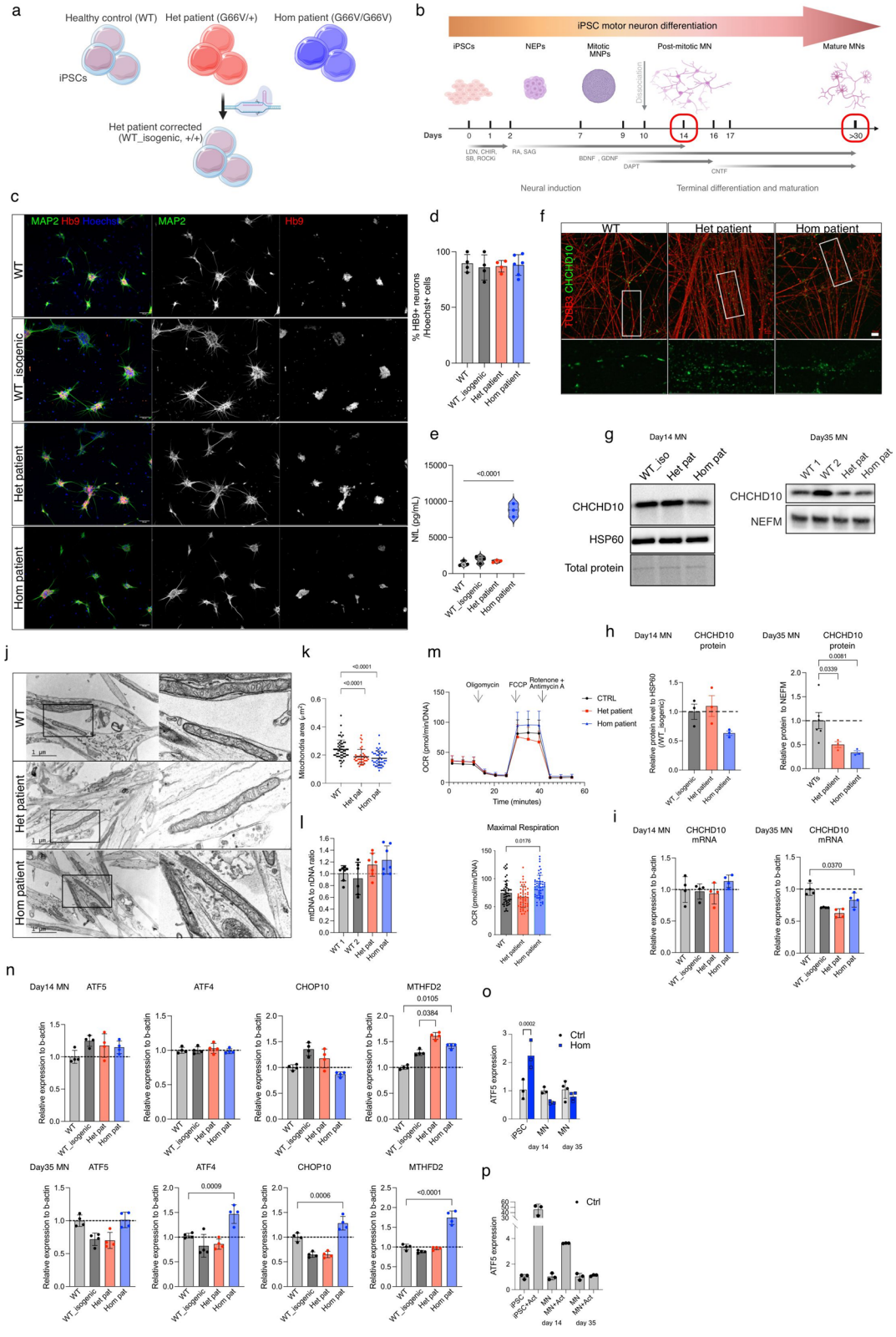

Fig. 3 (See legend on next page.)

(See figure on previous page.)

Fig. 3 mtISR induction is diminished upon motor neuron differentiation of patient-specific iPSC. (**A**) Diagram showing the cell lines used for motor neuron differentiation. (**B**) Diagram showing motor neuron differentiation protocol and timeline for sample collection. (**C**) Representative immunocytochemistry images showing positive staining for neuronal marker MAP2 (green) and motor neuronal marker HB9 (red) in d35-MN. Scale bar 50 µm. (**D**) Quantification of HB9-positive motor neurons in d35-MN. Total Hoechst-positive nuclei calculated in 4–6 independent fields of view/cell line (total $n = 140–412$ nuclei/cell line). (**E**) NfL amount in motor neuron culture media in d35-MN. (**F**) Representative immunocytochemistry image of staining with CHCHD10 (green) in neurites (TUBB3, red) antibodies in d35-MN. Scale bar 10 µm. (**G**) Immunoblotting of CHCHD10 at d14 and d35-MN from total cell lysates. (**H**) Quantification of CHCHD10 immunoblotting shows the results from three cultures per cell line, normalized to mitochondrial marker HSP60 (d14-MN, WT_isogenic used as control, $n = 3$/cell line) or neuronal marker NEFM (d35, 2 independent control cell lines, $n = 3$/cell line). (**I**) Expression of *CHCHD10* in d14 and d35-MN normalized to b-actin ($n = 4$/cell line). (**J**) Mitochondrial ultrastructure analysis by transmission electron microscopy in patient and control d35-MN. The right panel of each image is a magnification of the area indicated by the square in the left panel. Representative images of MN neurites are shown. Scale bars are indicated. (**K**) Quantification of mitochondrial area (μm^2) in electron micrographs (n = average area/image, 42–56 images/cell line). (**L**) mtDNA copy number was analyzed by qRT-PCR ($n = 6–7$ replicates/cell line). (**M**) Oxygen consumption rate (OCR) measurement in d35-MN using Seahorse XF96 Analyzer. Maximal respiration was assessed upon uncoupling with FCCP (two independent experiments with $n = 24–28$ replicates/run). (**N**) Expression of mtISR related transcripts (*ATF5*, *ATF4*, *CHOP10*, *MTHFD2)* in d14 and d35-MN normalized to b-actin ($n = 4$/cell line). (**O**) Expression of *ATF5* in control and homozygous iPSC, d14-MN and d35-MN ($n = 3$/genotype). (**P**) Expression of *ATF5* after treatment with actinonin in control iPSC, d14-MN and d35-MN ($n = 3$). Data shown relative to untreated condition (ethanol as vehicle). Data shown as mean ± standard deviation; $P < 0.05$ were considered significant by one-way ANOVA followed by Fisher's LSD's multiple comparison post-hoc test. Quantifications show all measured data points, results are presented relative to the average of all measured control data points

complexes showed less changes (supplemental Fig. 6A). In particular, the mtDNA-encoded subunit MT-CO1 and the assembly factor HIGD1A were increased, whereas HIGD2A and SMIM19 were decreased (Fig. 4G, H). Moreover, patient d14-MN displayed changes in proteins involved in iron homeostasis, with several cytosolic iron regulators being significantly increased while the mitochondrial factors were modestly decreased (Fig. 4I). Transferrin (TF) was one the most increased proteins (Fig. 4J, supplemental Fig. 4C). Also, the iron responsive element binding protein 2 (IREB2), which regulates iron levels in cells, the heme scavenger hemopexin (HPX), and the mitochondrial protein sideroflexin 5 (SFXN5) were increased in d14-MN of both patient cells (Fig. 4J). Notably, *SFXN5* mRNA expression was increased also in the dataset of CHCHD10 variant p.R15L fibroblasts (supplemental Fig. 5B, data from [36]). Moreover, the top significantly changed protein in heterozygous patient cells to its isogenic control comparison was apolipoprotein C3 (APOC3) (Fig. 4J, supplemental Fig. 4C).

In summary, patient-specific MN displayed considerable metabolic and proteomic changes during differentiation, at a time point when mitochondrial maturation takes place. Our findings suggest that in this critical period, CHCHD10 p.G66V variant may interfere with COX assembly and iron metabolism, and elevates creatine production.

Murine model of SMAJ tolerates the glycine to valine substitution well

We generated novel heterozygous and homozygous Chchd10 p.G66V (Chchd10^{G66V}, c.186G>T, p.G62V in mouse) mice with CRISPR/Cas9 editing (Fig. 5A). Successful knock-in generation was confirmed by DNA genotyping, and sequencing of *Chchd10* cDNA from muscle (Fig. 5A). Both heterozygous and homozygous Chchd10^{G66V} mice were viable and had normal life span (Fig. 5B, C). We monitored the weight of the mice until endpoint P550, and observed no differences between Chchd10^{G66V} and wild type animals (Fig. 5C). Muscle and fat mass, measured with EchoMRI, was unaltered in P550 Chchd10^{G66V} mice, indicating absence of substantial muscle atrophy (Fig. 5D), despite fatty tissue replacement being consistently found in SMAJ patient muscle [8]. Chchd10^{G66V} mice retained muscle strength and exercise endurance until the endpoint (Fig. 5E).

Since Chchd10^{S59L} and Chchd10^{G58R} mice present with lethal cardiomyopathy beginning already at the age of P150 [16, 17, 19], we assessed the cardiac function of Chchd10^{G66V} mice with echocardiography (supplemental Fig. 7A). At the age of 300 days, we could not detect aberrant cardiac function based on unaltered ejection fraction and fractional shortening in Chchd10^{G66V} mice. In addition, the morphology of the heart was normal, and the tissue did not show mtISR marker induction (supplemental Fig. 7B, C). We also investigated whether increased amount of insoluble CHCHD10 protein could be observed in heart tissue, as it is reported in other mutant Chchd10 mice. However, Chchd10^{G66V} mice did not show any detectable insoluble CHCHD10 in the heart tissue (supplemental Fig. 7D). Moreover, we did not observe increased insoluble CHCHD10 protein in patient cell models (supplemental Fig. 7E). These results confirm that Chchd10^{G66V} mice do not develop a similar cardiac phenotype as Chchd10^{S59L} and Chchd10^{G58R} mice.

Histopathological assessment of skeletal muscle indicated that Chchd10^{G66V} mice did not develop mitochondrial myopathy by P550: we did not observe COX-negative fibers (Fig. 5F). However, haematoxylin and eosin staining showed some changes in muscle fiber shape, namely increased circular muscle fibers (Fig. 5F, G), potentially indicating initial muscle pathology [44]. CK was not altered in Chchd10^{G66V} mouse serum (Fig. 5H). Mitochondrial morphology was normal

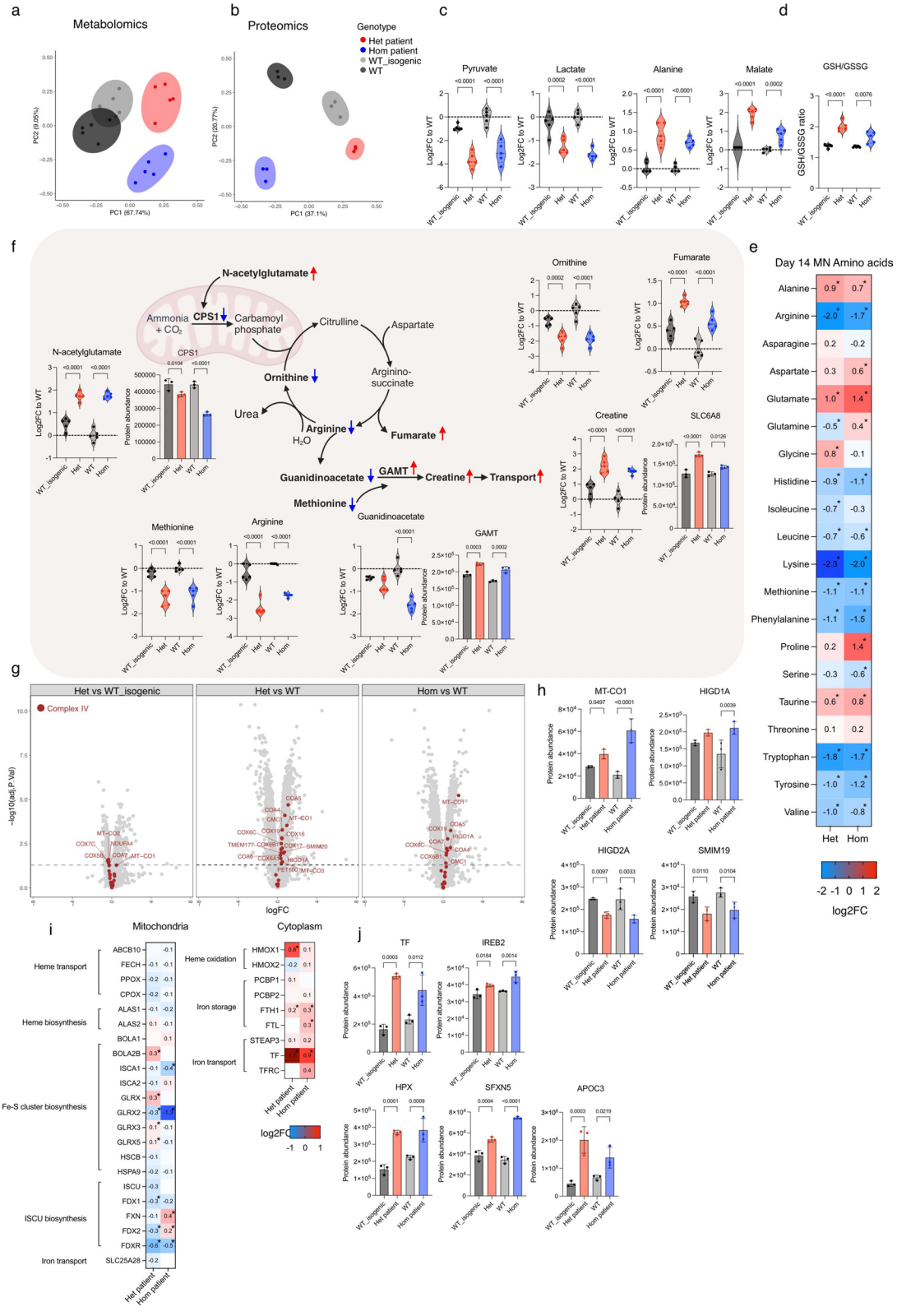

Fig. 4 (See legend on next page.)

(See figure on previous page.)

Fig. 4 Multiomics approach reveals metabolic remodeling and altered creatine pathway during motor neuron differentiation. (**A**) PCA showing overall differential metabolite abundances between patients and control d14-MN ($n=5$/cell line). (**B**) PCA showing overall differential protein abundances between patients and control d14-MN ($n=3$/cell line). (**C**) Pyruvate and lactate metabolite abundances are reduced, and alanine and malate are increased in patient d14-MN. (**D**) GSH/GSSG ratio determined from metabolomics data ($n=5$/cell line). (**E**) Heatmap of amino acids levels in heterozygous and homozygous d14-MN. ($n=5$/cell line, *adj.$p<0.05$, considered significant). (**F**) Schematic of metabolites and proteins associated with urea cycle and creatine metabolism. Red arrows indicate upregulation and blue arrows downregulation. (**G**) Volcano plots of OXPHOS CIV subunits and assembly factors (highlighted as red). (**H**) Protein abundancies of subunit mt-CO1 and assembly factors HIGD1A, HIGD2A and SMIM1 ($n=3$/cell line). (**I**) Heatmaps of mitochondrial and cytoplasmic proteins involved in iron metabolism ($n=3$/cell line). (**J**) Protein abundancies of TF, IREB2, HPX, SFXN5 and APOC3. Data represented as as log2(fold change) [log2(FC)] or as indicated. All comparisons are between heterozygous patient to WT_isogenic, and homozygous patient to WT. Data shown as mean ± standard deviation; *$p<0.05$ were considered significant by one-way ANOVA followed by Fisher's LSD's multiple comparison post-hoc test

in skeletal muscle at P365 by EM (Fig. 5I), and Chchd10^{G66V} mice had no mtDNA deletions in skeletal muscles at P550 (Fig. 5J, supplemental Fig. 8A). Similar to the patient fibroblasts and iPSC-MN, immunoblotting with CHCHD10 antibody showed a decreased CHCHD10 protein level in the skeletal muscles of the homozygous mice (60% reduction), however, heterozygous animals had normal CHCHD10 protein level (Fig. 5K, L). Next, we analyzed CHCHD10/CHCHD2 complexes in skeletal muscle with Native-PAGE (Fig. 5M), and used heart tissue from Chchd10^{S59L} mice as positive control for increased amount of higher molecular weight complexes, and from Chchd10^{G58R} mice as a negative control [20]. Homozygous Chchd10^{G66V} mice displayed reduced CHCHD10/CHCHD2 complexes in skeletal muscle (Fig. 5M). To further determine whether mutant CHCHD10 aggregated in Chchd10^{G66V} skeletal muscle, we applied a filter trap assay, which captures large detergent-insoluble protein aggregates. Chchd10^{G66V} mouse muscle (Fig. 5N) did not accumulate aggregated CHCHD10 or CHCHD2 unlike Chchd10^{S59L} mouse heart (Fig. 5N). Moreover, we did not observe OMA1-dependent OPA1 cleavage in Chchd10^{G66V} mouse muscle in contrast to Chchd10^{S59L} and Chchd10^{G58R} mouse heart (supplemental Fig. 8B).

Chchd10^{G66V} mouse offers insights into early disease stages

SMAJ is a relatively benign form of SMA, the Chchd10^{G66V} mice largely lacking any gross phenotype reflects the slow disease progression and late-onset in patients. However, Chchd10^{G66V} mice can elucidate the early disease development. Hindlimb clasping is an indicator of disease progression in several mouse models of neurodegeneration [45]. Therefore, we measured hindlimb clasping reflex in P550 Chchd10^{G66V} mice (Fig. 6A). Aged Chchd10^{G66V} mice showed more often the abnormal clasping phenotype when compared to wild type controls (Fig. 6A). Since hindlimb clasping could be an indicator of motor dysfunction, we assessed motor neuronal function with compound muscle action potential (CMAP) measurement (Fig. 6B). Chchd10^{G66V} mice showed similar neuronal function as wild type littermates at age of P550 determined by amplitude, latency, and nerve conduction velocity (Fig. 6B). Also, lumbar spinal cord morphology was comparable to wild type mice and no signs of spinal motor neuron loss was present (Fig. 6C). Moreover, the amount of NfL was not changed in Chchd10^{G66V} mouse serum (Fig. 6D). Although the P550 Chchd10^{G66V} mice displayed normal exercise performance and unaltered motor neuron function, we observed a reduction in neuromuscular junction area (Fig. 6E, F). Additionally, 30% of the neuromuscular junctions in homozygous mice showed fragmentation. Interestingly, CHCHD10 protein level was reduced (50% reduction) in Chchd10^{G66V} homozygous mouse spinal cord (Fig. 6G, H, supplemental Fig. 8C), and also slightly in heterozygotes (20% reduction), which had normal CHCHD10 level in skeletal muscle. These findings indicate that p.G66V variant affects the stability of CHCHD10 protein in a tissue-specific manner in mice.

Finally, we studied serum and muscle metabolite profiles, and skeletal muscle transcriptomics to identify whether Chchd10^{G66V} mice had any subtle abnormalities despite the overall normal appearance. Principal component analysis indicated no major changes occurring in serum or muscle metabolome or muscle transcriptome in P550 mice unlike in patient cell models (Fig. 6I-J, supplemental Fig. 8D). Furthermore, the expression of mtISR markers (*Fgf21* or *Gdf15*) was not induced (supplemental Fig. 8E). These results show that at this stage of disease progression there are no signs of mitochondrial myopathy or changes in creatine metabolism. However, we observed increased expression of a subset of transcripts that were related to inflammatory response in homozygous Chchd10^{G66V} mice (Fig. 6K). Notably, the expression of inflammatory cytokines and receptors *Cxcl13*, *Cxcr4*, *Cxcr5*, and *Cd19* were increased (Fig. 6L).

Our findings indicate that the variant equivalent to p.G66V is well tolerated in mice, even in homozygous state. There is a tissue-specific reduction in CHCHD10 amount, mimicking the findings in human cell models, and no aggregates. The Chchd10^{G66V} mice are largely lacking any noticeable phenotype, although initial pathology affecting the neuromuscular junctions may be

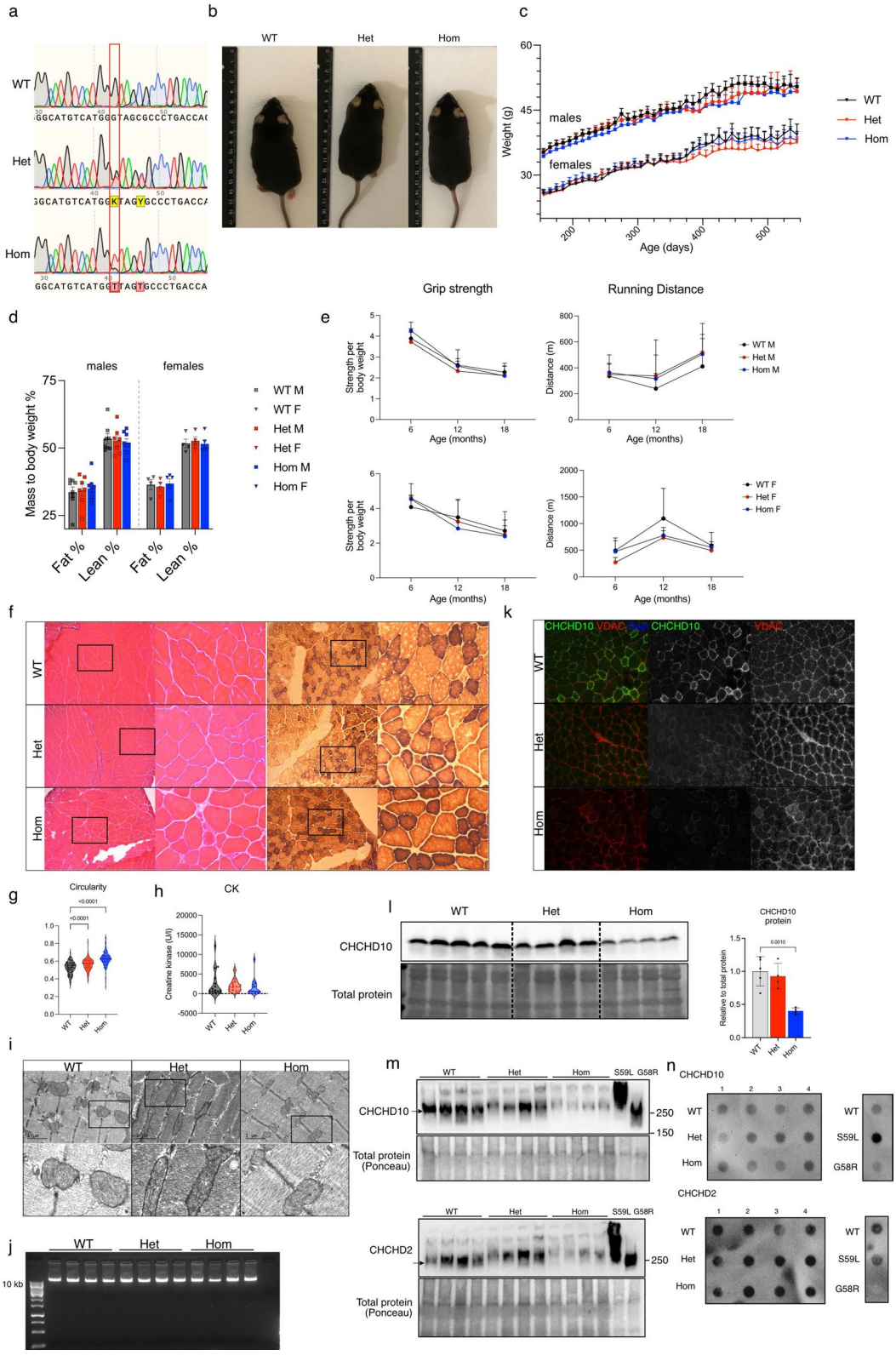

Fig. 5 (See legend on next page.)

(See figure on previous page.)

Fig. 5 Homozygous Chchd10^{G66V} mice show loss of CHCHD2/CHCHD10 complexes in muscle but do not develop mitochondrial myopathy. (**A**) Generation of p.G66V (p.G62V in mouse) knockin mice was confirmed by sequencing of cDNA from muscle. Red box indicates the site c.186 G→T (p.G62V) (in human c.197 G→T, p.G66V) mutation introduced by gene editing in the *Chchd10* gene. (**B**) Heterozygous and homozygous Chchd10^{G66V} mice have a normal appearance at P365. (**C**) Body weight curve of male and female mice until P550 (n = 21/genotype, male; n = 15/genotype, female). (**D**) Fat and lean mass normalized to body weight measured with EchoMRI at P550 (n = 7–8/genotype, males; n = 4–5, females). (**E**) Grip strength (N/g) normalized to body weight. Exercise endurance assessed with treadmill indicated as the distance travelled (m) until fatigue. Time points for measurements 6, 12, and 18 months (n = 5–7/genotype/timepoint, males; n = 4–7/genotype/timepoint, females). Upper panels represent male mice, lower panels female mice. (**F**) Representative histological stainings from P550 quadriceps femoris (QF) muscle. Left panel H&E staining, middle panel COX-SDH activity. Black box indicates a magnification of the area indicated shown in the left panel. Scale bar 100 µm. (**G**) Quantification of circularity (0–1/fiber) of muscle fibers from H&E stained QF muscle (n = 3–4/genotype/sex, 94–190 fibers/animal). (**H**) Creatine kinase (CK) levels in P550 mouse serum (n = 6–7/genotype, males; n = 5/genotype, females). (**I**) Transmission electron micrograph of QF muscle. (**J**) Long-range PCR of mouse QF muscle for mtDNA deletions at P550 (n = 4/genotype). (**K**) Representative immunohistochemistry with CHCHD10 (green) and VDAC/porin (red) antibodies of QF muscle. (**L**) Immunoblotting and quantification with CHCHD10 antibody from QF muscle normalized to total protein (n = 4–5/genotype). (**M**) Native-PAGE and immunoblotting with CHCHD10 and CHCHD2 antibodies from QF muscle (n = 4/genotype). Chchd10^{S59L} and Chchd10^{G58R} heart used as positive and negative control for aggregation, respectively. Total protein shown as loading control. (**N**) Filter trap with CHCHD10 and CHCHD2 antibodies from QF muscle lysates. Chchd10^{S59L} and Chchd10^{G58R} heart used as positive and negative control for aggregation, respectively. Data shown as mean ± standard deviation; $P < 0.05$ were considered significant by one-way ANOVA followed by Fisher's LSD's multiple comparison post-hoc test. Quantifications show all measured data points, results are presented relative to the average of all measured WT values

starting to emerge, as well as first signs of neuroinflammation at the age of P550.

Discussion

The pathogenic mechanisms in *CHCHD10*-related disorders as well as the normal function of CHCHD10 protein in mitochondria are incompletely understood. Nevertheless, CHCHD10 seems to be important for the proper functioning of motor nerves, given the motor neuron phenotypes caused by many of the CHCHD10 disease variants. Here, we describe the first homozygous CHCHD10 patient, with the SMAJ p.G66V variant, and provide the first detailed analysis of consequences of heterozygous and homozygous p.G66V variants *in vitro* and *in vivo*. Our results highlight changes in redox state and creatine pathway in SMAJ cell models, proposing that increased serum creatine levels in SMAJ patients may arise from primary involvement of CHCHD10 in creatine metabolism.

All reported pathogenic mutations in *CHCHD10* have so far been heterozygous in either sporadic patients or dominant pedigrees. The phenotype of the p.G66V homozygous patient was similar to the well-characterized heterozygous individuals [8, 9], although with much earlier onset resulting in severe disability already before the typical age of onset in heterozygous cases. Moreover, the homozygous patient has a mitochondrial myopathy with multiple mtDNA deletions and COX-negative and ragged-red muscle fibers, indicating that muscle involvement and the overall disease severity in patients with the p.G66V mutation depend on mutation dosage. The disease-related abnormalities of the homozygous patient were strictly confined to the neuromuscular system and a multi-organ involvement present in many other mitochondrial disorders was not found. Our results show that a biallelic variant in *CHCHD10* causes a more severe SMAJ phenotype than the same variant in heterozygous state. Nevertheless, the disease course was slowly progressive and did not clinically resemble ALS.

Previous investigation of patient-derived cells indicated that the heterozygous p.G66V variant did not affect *CHCHD10* mRNA expression but resulted in 50% reduced protein level [22]. Thus, the p.G66V was proposed to cause motor neuron disease through haploinsufficiency. Our findings partly align with the previous study; however, the reduction in CHCHD10 protein level varied across our different in vitro and in vivo models. Yet the biggest reduction was always found in models carrying the homozygous variant in comparison to the heterozygous. We did not observe a complete loss of CHCHD10 in homozygous models, arguing against pure haploinsufficiency, and enabling that the residual dysfunctional mutant CHCHD10 could have toxic effects. Structural modelling has predicted that the p.G66V variant does not increase the aggregation probability of CHCHD10 [23]. Our findings support this notion, as we did not observe aggregation or increased insolubility of the p.G66V mutant protein in our models. However, the lack of protein aggregation does not exclude misfolding of the mutant protein and aberrant protein interactions. In conclusion, our results demonstrate that the p.G66V variant leads to dose-dependent reduction of the CHCHD10 protein, but the disease mechanism could involve a toxic gain-of-function of the mutant protein, which in the homozygous state is doubled. The amount of the remaining mutant CHCHD10 in different cell types may depend on the expression level of CHCHD2 or other proteins participating in complex formation with CHCHD10.

Despite the lack of CHCHD10 aggregates, we observed increased mtISR marker expression in patient fibroblasts, consistently in a dose-dependent manner. This was perhaps unexpected as our earlier study of SMAJ patients' serum samples showed normal levels of FGF21 and

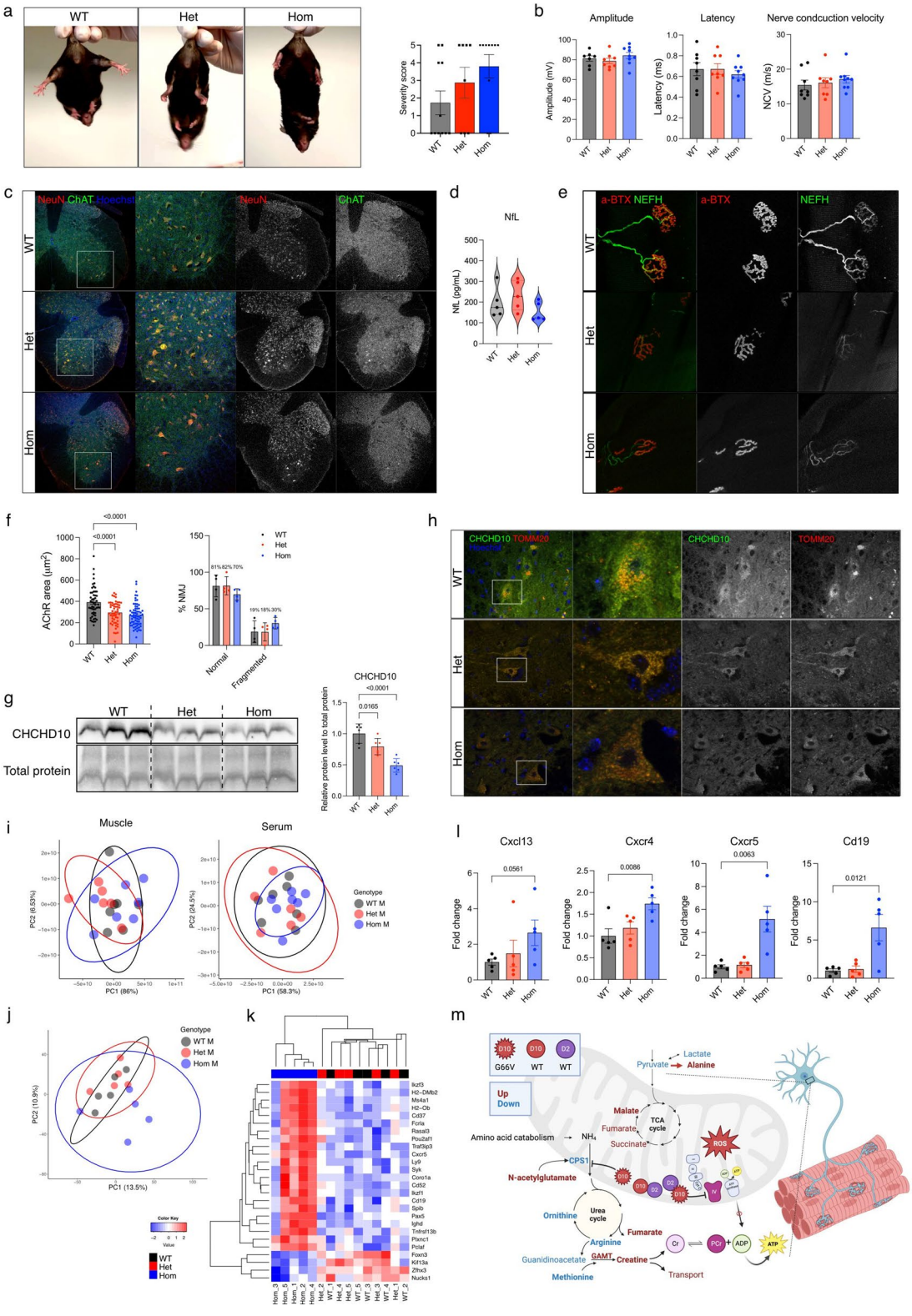

Fig. 6 (See legend on next page.)

(See figure on previous page.)

Fig. 6 Chchd10^{G66V} mice show initial neuromuscular pathology and inflammatory response in muscle. (**A**) Motor performance assessed with hindlimb clasping test in P550 mice. Representative images of clasping test and performance rated by severity score ($n = 5$–7/genotype, males; $n = 3$–4/genotype, females). (**B**) Compound muscle action potentials (CMAP) measured from gastrocnemius muscle upon stimulation of sciatic nerve at P550. Amplitude (mV), latency (ms) and nerve conduction velocity (m/s) shown ($n = 7$–9/genotype). (**C**) Representative immunohistochemistry image of lumbar spinal cord stained with NeuN (red) and ChAT (green) antibodies. (**D**) NfL levels in mouse serum at P550 ($n = 5$/genotype). (**E**) Representative immunohistochemistry image of neuromuscular junction. Acetylcholine receptors stained with a-BTX (red) and nerve with NEFH (green) antibodies. (**F**) Quantification of acetylcholine receptor area (a-BTX positive area) and percentage of fragmented neuromuscular junctions in all imaged fields ($n = 4$ animals/genotype, 11–21 neuromuscular junctions/animal). (**G**) Immunoblotting and quantification of CHCHD10 in mouse spinal cord. Quantification shows $n = 6$/genotype (3 females, 3 males). (**H**) Representative immunohistochemistry of lumbar spinal cord, stained with mitochondrial marker TOMM20 (red), and CHCHD10 (green) antibodies. (**I**) PCA showing overall metabolite profile between WT and Chchd10^{G66V} mice in muscle and serum ($n = 6$–7/genotype, males). (**J**) PCA showing overall gene expression profile between WT and Chchd10^{G66V} mice in muscle ($n = 5$/genotype, males). (**K**) Heatmap showing top 25 significantly changed transcripts in homozygous Chchd10^{G66V} mouse muscle. (**L**) Expression of *Cxcl13*, *Cxcr4*, *Cxcr5* and *Cd19* in Chchd10^{G66V} mouse muscle. Data shown as relative to control expression ($n = 5$/genotype). (**M**) Illustration of the proposed pathogenic effects of CHCHD10 p.G66V variant. Data shown as mean ± standard deviation; $P < 0.05$ were considered significant by one-way ANOVA followed by Fisher's LSD's multiple comparison post-hoc test

GDF15 [11], indicating that mtISR cannot be prominent in patient tissues. In other CHCHD10 models, mtISR activation by the OMA1-DELE1-HRI pathway has been demonstrated in association with the aggregation of p.S59L and p.G58R variants, as well as in the CHCHD10/CHCHD2 double knockout mice [15–17, 19, 20]. Interestingly, induced mtISR marker expression in patient fibroblasts, particularly *ATF5*, was lost during MN differentiation, which we propose to owe to the requirement of ATF5 downregulation to allow neuronal maturation [43]. This finding highlights the dependence of mtISR induction on the cell type and its transcriptional program, and prompts the question whether mtISR is protective for some cell types, given the limited tissue involvement in SMAJ. DELE1-mediated mtISR activation has been shown to be protective in Chchd10^{S59L} and Chchd10^{G58R} mice, in which knocking out DELE1 dramatically decreased the survival of the mutant mice [46], emphasizing the protective nature of mtISR activation upon mitochondrial stress.

To investigate the protein level changes caused by the p.G66V variant, we focused our analysis on the time point of MN differentiation (d14-MN) that showed the most metabolic differences. This developmental stage is critical for the maturation of the OXPHOS (Torregrosa-Muñumer et al. unpublished observations, manuscript in preparation). Interestingly, we observed changes in the protein amounts of OXPHOS CIV subunit MT-CO1, and assembly factors HIGD1A, HIGD2A and SMIM19. Several studies have suggested interactions between CHCHD10 and CIV or modulation of CIV activity by CHCHD10 [47–50]. Moreover, *CHCHD10* mutants p.G66V and p.P80L displayed defective interactions with CHCHD2 and COX, leading to reduced respiration and increased production of reactive oxygen species (ROS) in cancer cells [50]. We also observed reduced maximal respiration and redox imbalance, as shown by altered NADPH/NADP + and GSH/GSSG ratios, in heterozygous patient fibroblasts and d14-MN. We hypothesize that CHCHD10 availability could affect CIV assembly or function in a manner that is most evident in specific cells or developmental stages. The d14-MN proteome also displayed increases in several proteins regulating iron and heme homeostasis and iron-sulfur cluster biogenesis (TF, IREB2, HPX and SFXN5). The involvement of CHCHD10/CHCHD2 in regulating iron homeostasis is supported by our previous investigations [24] and those of others [19, 51]. Notably, loss of CHCHD10 or CHCHD2 has been shown to affect intramitochondrial iron content and gene expression of iron transporter *TF* [24, 51]. We noted that *SFXN5* expression was increased also in CHCHD10 p.R15L fibroblasts [36]. Interestingly, another sideroflexin family protein, SFXN1, has been reported to physically interact with CHCHD10 [52]. These changes in the iron, heme and OXPHOS related proteins, now detected in multiple independent models, strongly link the function of CHCHD10 to these pathways.

Importantly, our metabolomic and proteomic analysis of d14-MN emphasized changes in the urea cycle and creatine metabolism. Creatine has been shown to be important for nervous system bioenergetics since it replenishes ATP without the need of oxygen [53]. Mitochondrial network is required to transduce energy over long distances; for example, in long axons, whereas cells with a disrupted mitochondrial network might need to buffer energy via the creatine kinase–phosphocreatine circuit [54]. Thus, creatine has been shown to be important for neuronal function due to its buffering ability to provide energy quickly for high energy demanding neuronal tissue [55]. Creatine is produced from arginine and glycine by the enzyme GATM. In d14-MN the urea cycle catalyzing enzyme, CPS1, was decreased, whereas its' allosteric activator, N-acetylglutamate, was increased. Moreover, metabolites downstream of CPS1 (ornithine, arginine, methionine and guanidinoacetate) were decreased, whereas GAMT, creatine and creatine transporter were increased. We propose that the reduction of precursors and increased end-products indicate rewiring of creatine metabolism in p.G66V d14-MN to bypass increased energy requirements of maturing motor neurons when conventional mitochondrial energy production is slightly

dysfunctional. These results suggest that altered creatine metabolism could be a primary mechanism associated with the p.G66V variant. Mitochondrially located *CPS1* expression was also downregulated in CHCHD10 p.R15L fibroblasts that show a reduced CHCHD10 level [36], further hinting that CHCHD10 amount and CPS1 activity might be co-regulated. One carbon metabolism, altered in many CHCHD10 models [19, 36], is also intricately linked to creatine metabolism through their shared use of methyl groups. Interest in creatine biology has been developing, with new insights into a diverse set of regulatory functions for creatine. Creatine has also been reported as a potent neuroprotective agent and antioxidant [56], and creatine supplementation as a possible treatment to alleviate neurodegenerative diseases [57]. Moreover, creatine was recently suggested to function as a novel inhibitory neurotransmitter [58]. Future research will show whether modulation of creatine metabolism could offer possible treatment avenues for SMAJ. This direction is supported by CK being typically elevated in SMAJ serum, and by the positive correlation between serum creatine levels and disease severity [11].

In this study we developed a novel mouse model for the p.G66V variant. The amino acid change was well-tolerated in mice, in contrast to the previously reported p.S59L and p.G58R mice. CHCHD10 protein level was faithfully reduced in Chchd10^{G66V} mouse muscle and spinal cord, following dose-dependency, similarly to our human in vitro models. Muscle involvement was more prominent in homozygous mice, as shown by reduced CHCHD10/CHCHD2 complexes in muscle. Chchd10^{G66V} mice retained muscle strength and exercise endurance until 18 months of age, whereas Chchd10^{S59L} mice exhibited motor dysfunction initiating at the age of 8 months [16, 17]. Notably, Chchd10^{G66V} mice did not develop a cardiac phenotype, unlike Chchd10^{S59L} and Chchd10^{G58R} mice, supporting a different disease mechanism of the p.G66V variant. Interestingly, Chchd10^{G66V} mice showed initial changes in neuromuscular junctions. This finding is in line with a recent zebrafish study, which proposed that CHCHD10 could be involved in neuromuscular junction stability [59], and with the muscle-specific conditional CHCHD10 knockout mice that showed CHCHD10 is required for acetylcholine receptor clustering in neuromuscular junctions [25]. Furthermore, we observed that aged homozygous Chchd10^{G66V} mice displayed initial transcriptional upregulation of inflammatory signaling. Interestingly, neuroinflammation was recently reported in aged heterozygous Chchd10^{S59L} mice [18]. Thus, initial pathology affecting the neuromuscular junctions may be starting to emerge in Chchd10^{G66V} mice, as well as the first signs of neuroinflammation. Since SMAJ is a relatively benign form of SMA, the Chchd10^{G66V} mice largely lacking any gross phenotype could actually reflect the slow disease progression and late-onset in patients. However, the mild phenotype of the Chchd10^{G66V} mice complicates their utilization in studying disease mechanisms and in treatment trials.

Conclusions

In conclusion, we have established a number of new human and mouse models of p.G66V, and characterized their feasibility for uncovering molecular and metabolic mechanisms of SMAJ. Our results show that the p.G66V variant leads to reduction of the mutant CHCHD10 protein amount, but not its complete loss even in the homozygous state, therefore the mutant CHCHD10 could have a toxic gain-of-function role. The disease variant likely alters the ability of CHCHD10 to interact with proteins that are involved in maintaining redox balance, iron/heme homeostasis, CIV function and creatine metabolism (Fig. 6M), offering strategies for interventions.

Supplementary Information

The online version contains supplementary material available at https://doi.org/10.1186/s40478-025-02039-3.

Supplementary Material 1
Supplementary Material 2
Supplementary Material 3
Supplementary Material 4
Supplementary Material 5
Supplementary Material 6
Supplementary Material 7
Supplementary Material 8

Acknowledgements

Jana Pennonen, Miia Nissilä, and Juhana Juutila are thanked for assistance and expert support. The services by Biomedicum Imaging Unit, Genetically Modified Rodents Unit of the Laboratory Animal Center University of Helsinki, Electron Microscopy Unit of the Institute of Biotechnology, Biomedicum Functional Genomics Unit, Turku Proteomics Facility supported by Biocenter Finland, Ninna Koho and University of Helsinki Animal Hospital laboratory (YESLAB) are acknowledged for their services and collaborations. In addition, we acknowledge Biomag and Juha Montonen for CMAP equipment. Schematic figures were created with BioRender.com. This study has been funded by the Research Council of Finland Centre of Excellence on Stem Cell Metabolism, Sigrid Juselius Foundation, Magnus Ehrnrooth Foundation, Emil Aaltonen Foundation, Orion Research Foundation, Biomedicum Helsinki Foundation, Päivikki and Sakari Sohlberg Foundation, Paulo Foundation, Finnish-Norwegian Medicine Foundation, University of Helsinki, and Helsinki University Hospital.

Author contributions

Conceptualization– S.H., M.J., E.Y., H.T.; Methodology and Investigation– S.H., J.R., B.H., M.R., L.K., K.H., L.E., E.P., F.Z., T.Z., S.K., N.H., SK.H., A.H., E.K., V.H., T.B, L.V.D.B; Formal analysis– S.H., J.R., J.K.; Resources– X.H., D.N.; Writing– Original Draft Preparation S.H. and H.T.; Writing– Review & Editing, all authors; Project Administration H.T.; Funding Acquisition E.Y. and H.T.; Supervision, V.H., L.V.D.B, P.K., S.K., E.Y. and H.T.

Funding
Open Access funding provided by University of Helsinki (including Helsinki University Central Hospital).
This study has been funded by the Research Council of Finland Centre of Excellence on Stem Cell Metabolism, Sigrid Juselius Foundation, Magnus Ehrnrooth Foundation, Emil Aaltonen Foundation, Orion Research Foundation, Biomedicum Helsinki Foundation, Päivikki and Sakari Sohlberg Foundation, Paulo Foundation, Finnish-Norwegian Medicine Foundation, University of Helsinki, and Helsinki University Hospital.

Data availability
Values for all data points in graphs are reported in the Supporting Data Values file. The RNAseq data generated in this study have been deposited in the NCBI's Gene Expression Omnibus (GEO) database (accession number; GSE276449). Proteomics data have been deposited in the MassIVE database (accession number; MSV000095780). Metabolomics data have been submitted to the Metabolomics Workbench database (accession number; PR002145).

Declarations

Ethics approval and consent to participate
Animal experiments were performed in compliance with the national ethical guidelines set by the European Union and were approved by the National Animal Experiment Board (Project Authorisation Board, project license ESAVI-12691-2021). The ethical practice of handling laboratory animals was strictly followed throughout the procedures. The generation of the human induced pluripotent stem cell lines used in this study was approved by the Coordinating Ethics Committee of the Helsinki and Uusimaa Hospital District (Nro 423/13/03/00/08) with informed consent of the donor.

Consent for publication
Written and informed consent of patient was received prior examination for results and the usage of photographs for publication.

Competing interests
The authors declare that they have known competing financial interests or personal relationships that could have appeared to influence the work reported in this paper. L.E. is a co-founder of NADMED Ltd. L.V.D.B. is the scientific founder of Augustine Therapeutics and is head of the Scientific Advisory Board. L.V.D.B. is also part of the Investment Advisory Board of Droia Ventures (Meise, Belgium). Authors declare no other conflicts of interest.

Author details
[1]Stem Cells and Metabolism Research Program, Faculty of Medicine, University of Helsinki, Helsinki, Finland
[2]Clinical Neurosciences, University of Turku and Neurocenter, and Turku University Hospital, Turku, Finland
[3]Neuromuscular Research Center, Tampere University Hospital and Tampere University, Tampere, Finland
[4]GM-unit, Helsinki Institute of Life Science (HiLIFE), University of Helsinki, Helsinki, Finland
[5]Research Program for Clinical and Molecular Metabolism, Faculty of Medicine, University of Helsinki, Helsinki, Finland
[6]Research Unit of Biomedicine and Internal Medicine, Faculty of Medicine, University of Oulu, Oulu, Finland
[7]Medical Research Center Oulu, Oulu University Hospital and University of Oulu, Oulu, Finland
[8]Biocenter Oulu, University of Oulu, Oulu, Finland
[9]A.I. Virtanen Institute for Molecular Sciences, University of Eastern Finland, Kuopio, Finland
[10]Department of Neurology, Kuopio University Hospital, Kuopio, Finland
[11]Institute of Clinical Medicine, Neurology, University of Eastern Finland, Kuopio, Finland
[12]Institute of Biotechnology, HiLIFE, University of Helsinki, Helsinki, Finland
[13]Faculty of Biological and Environmental Sciences, University of Helsinki, Helsinki, Finland
[14]Department of Cell and Molecular Biology, Karolinska Institutet, Stockholm, Sweden
[15]Department of Neurosciences, Experimental Neurology and Leuven Brain Institute, KU Leuven, Leuven, Belgium
[16]VIB Center for Brain & Disease Research, Laboratory of Neurobiology, VIB-KU Leuven, Leuven, Belgium
[17]Mitochondrial Biology and Neurodegeneration Unit, Neurogenetics Branch, National Institute of Neurological Disorders and Stroke, National Institutes of Health, Bethesda, MD 20892, USA
[18]Clinical Neurosciences, Neurology, Helsinki University Hospital, Helsinki, Finland
[19]Department of Medical and Clinical Genetics, University of Helsinki, Helsinki, Finland
[20]Biomedicum Helsinki, r.C525b, Haartmaninkatu 8, Helsinki 00290, Finland

Received: 21 February 2025 / Accepted: 12 May 2025
Published online: 22 May 2025

References

1. Bannwarth S, Ait-El-Mkadem S, Chaussenot A, Genin EC, Lacas-Gervais S, Fragaki K, Berg-Alonso L, Kageyama Y, Serre V, Moore DG, Verschueren A, Rouzier C, Le Ber I, Augé G, Cochaud C, Lespinasse F, N'guyen K, De Septenville A, Brice A, Yu-Wai-Man P, Sesaki H, Pouget J, Paquis-Flucklinger V (2014) A mitochondrial origin for frontotemporal dementia and amyotrophic lateral sclerosis through CHCHD10 involvement. Brain 137:2329–2345. https://doi.org/10.1093/brain/awu138
2. Chaussenot A, Le Ber I, Ait-El-Mkadem S, Camuzat A, de Septenville A, Bannwarth S, Genin EC, Serre V, Augé G, Brice A, Pouget J, Paquis-Flucklinger V (2014) Screening of CHCHD10 in a French cohort confirms the involvement of this gene in frontotemporal dementia with amyotrophic lateral sclerosis patients. Neurobiol Aging 35:2884e1–2884e4. https://doi.org/10.1016/j.neurobiolaging.2014.07.022
3. Consortium PMALSS (2018) CHCHD10 variants in amyotrophic lateral sclerosis: where is the evidence? Ann Neurol 84:110–116. https://doi.org/10.1002/ana.25273
4. Johnson JO, Glynn SM, Gibbs JR, Nalls MA, Sabatelli M, Restagno G, Drory VE, Chiò A, Rogaeva E, Traynor BJ (2014) Mutations in the CHCHD10 gene are a common cause of Familial amyotrophic lateral sclerosis. Brain 137:e311
5. Müller K, Andersen PM, Hübers A, Marroquin N, Volk AE, Danzer KM, Meitinger T, Ludolph AC, Strom TM, Weishaupt JH (2014) Two novel mutations in conserved codons indicate that CHCHD10 is a gene associated with motor neuron disease. Brain 137:e309
6. Ronchi D, Riboldi G, Del Bo R, Ticozzi N, Scarlato M, Galimberti D, Corti S, Silani V, Bresolin N, Comi G, Pietro (2015) CHCHD10 mutations in Italian patients with sporadic amyotrophic lateral sclerosis. Brain 138:e372
7. Ajroud-Driss S, Fecto F, Ajroud K, Lalani I, Calvo SE, Mootha VK, Deng HX, Siddique N, Tahmoush AJ, Heiman-Patterson TD, Siddique T (2014) Mutation in the novel nuclear-encoded mitochondrial protein CHCHD10 in a family with autosomal dominant mitochondrial myopathy. Neurogenetics 16:1–9. https://doi.org/10.1007/s10048-014-0421-1
8. Jokela M, Penttilä S, Huovinen S, Hackman P, Saukkonen AM, Toivanen J, Udd B (2011) Late-onset lower motor neuronopathy: A new autosomal dominant disorder. Neurology 77:334–340. https://doi.org/10.1212/WNL.0b013e3182267b71
9. Penttilä S, Jokela M, Bouquin H, Saukkonen AM, Toivanen J, Udd B (2015) Late onset spinal motor neuronopathy is caused by mutation in CHCHD10. Ann Neurol 77:163–172. https://doi.org/10.1002/ana.24319
10. Shammas MK, Huang T-H, Narendra DP (2023) CHCHD2 and CHCHD10-related neurodegeneration: molecular pathogenesis and the path to precision therapy. Biochem Soc Trans 51:797–809. https://doi.org/10.1042/BST20221365
11. Järvilehto J, Harjuhaahto S, Palu E, Auranen M, Kvist J, Zetterberg H, Koskivuori J, Lehtonen M, Saukkonen AM, Jokela M, Ylikallio E, Tyynismaa H (2022) Serum creatine but not neurofilament light is elevated in CHCHD10-linked spinal muscular atrophy. Front Neurol 0:96. https://doi.org/10.3389/FNEUR.2022.793937
12. Jokela M, Huovinen S, Raheem O, Lindfors M, Palmio J, Penttilä S, Udd B (2016) Distinct muscle biopsy findings in genetically defined Adult-Onset motor neuron disorders. PLoS ONE 11:e0151376. https://doi.org/10.1371/JOURNAL.PONE.0151376
13. Genin EC, Bannwarth S, Ropert B, Lespinasse F, Mauri-Crouzet A, Augé G, Fragaki K, Cochaud C, Donnarumma E, Lacas-Gervais S, Wai T, Paquis-Flucklinger V (2022) CHCHD10 and SLP2 control the stability of the PHB complex:

A key factor for motor neuron viability. Brain 145:3415–3430. https://doi.org/10.1093/brain/awac197
14. Zhou W, Ma D, Sun AX, Tran HD, Ma DL, Singh BK, Zhou J, Zhang J, Wang D, Zhao Y, Yen PM, Goh E, Tan EK (2019) PD-linked CHCHD2 mutations impair CHCHD10 and MICOS complex leading to mitochondria dysfunction. Hum Mol Genet 28:1100–1116. https://doi.org/10.1093/hmg/ddy413
15. Liu YT, Huang X, Nguyen D, Shammas MK, Wu BP, Dombi E, Springer DA, Poulton J, Sekine S, Narendra DP (2020) Loss of CHCHD2 and CHCHD10 activates OMA1 peptidase to disrupt mitochondrial Cristae phenocopying patient mutations. Hum Mol Genet 29:1547–1567. https://doi.org/10.1093/hmg/ddaa077
16. Anderson CJ, Bredvik K, Burstein SR, Davis C, Meadows SM, Dash J, Case L, Milner TA, Kawamata H, Zuberi A, Piersigilli A, Lutz C, Manfredi G (2019) ALS/FTD mutant CHCHD10 mice reveal a tissue-specific toxic gain-of-function and mitochondrial stress response. Acta Neuropathol. https://doi.org/10.1007/s00401-019-01989-y
17. Genin EC, Madji Hounoum B, Bannwarth S, Fragaki K, Lacas-Gervais S, Mauri-Crouzet A, Lespinasse F, Neveu J, Ropert B, Augé G, Cochaud C, Lefebvre-Omar C, Bigou S, Chiot A, Mochel F, Boillée S, Lobsiger CS, Bohl D, Ricci JE, Paquis-Flucklinger V (2019) Mitochondrial defect in muscle precedes neuromuscular junction degeneration and motor neuron death in CHCHD10 S59L/+ mouse. Acta Neuropathol 138:123–145. https://doi.org/10.1007/s00401-019-01988-z
18. Genin EC, di Borgo PP, Lorivel T, Hugues S, Farinelli M, Mauri-Crouzet A, Lespinasse F, Godin L, Paquis-Flucklinger V, Petit-Paitel A (2024) CHCHD10S59L/+ mouse model: behavioral and neuropathological features of frontotemporal dementia. Neurobiol Dis 106498. https://doi.org/10.1016/j.nbd.2024.106498
19. Sayles NM, Southwell N, McAvoy K, Kim K, Pesini A, Anderson CJ, Quinzii C, Cloonan S, Kawamata H, Manfredi G (2022) Mutant CHCHD10 causes an extensive metabolic rewiring that precedes OXPHOS dysfunction in a murine model of mitochondrial cardiomyopathy. Cell Rep 38. https://doi.org/10.1016/j.celrep.2022.110475
20. Shammas MK, Huang X, Wu BP, Fessler E, Song IY, Randolph NP, Li Y, Bleck CK, Springer DA, Fratter C, Barbosa IA, Powers AF, Quirós PM, Lopez-Otin C, Jae LT, Poulton J, Narendra DP (2022) OMA1 mediates local and global stress responses against protein misfolding in CHCHD10 mitochondrial myopathy. J Clin Invest 132. https://doi.org/10.1172/JCI157504
21. Costa-Mattioli M, Walter P (2020) The integrated stress response: from mechanism to disease. Science 368. https://doi.org/10.1126/SCIENCE.AAT5314/ASSET/920D0C5B-D818-48A6-8F68-0963BB9D3030/ASSETS/GRAPHIC/368_AAT5314_F4.JPEG
22. Brockmann SJ, Freischmidt A, Oeckl P, Müller K, Ponna SK, Helferich AM, Paone C, Reinders J, Kojer K, Orth M, Jokela M, Auranen M, Udd B, Hermann A, Danzer KM, Lichtner P, Walther P, Ludolph AC, Andersen PM, Otto M, Kursula P, Just S, Weishaupt JH (2018) CHCHD10 mutations P. R15L and P. G66V cause motoneuron disease by haploinsufficiency. Hum Mol Genet 27:706–715. https://doi.org/10.1093/hmg/ddx436
23. Alici H, Uversky VN, Kang DE, Woo JA, Coskuner-Weber O (2023) Effects of the Jokela type of spinal muscular atrophy-related G66V mutation on the structural ensemble characteristics of CHCHD10. Proteins Struct Funct Bioinform 91:739–749. https://doi.org/10.1002/prot.26463
24. Harjuhaahto S, Rasila TS, Molchanova SM, Woldegebriel R, Kvist J, Konovalova S, Sainio MT, Pennonen J, Torregrosa-Muñumer R, Ibrahim H, Otonkoski T, Taira T, Ylikallio E, Tyynismaa H (2020) ALS and Parkinson's disease genes CHCHD10 and CHCHD2 modify synaptic transcriptomes in human iPSC-derived motor neurons. Neurobiol Dis 141. https://doi.org/10.1016/j.nbd.2020.104940
25. Xiao Y, Zhang J, Shu X, Bai L, Xu W, Wang A, Chen A, Tu W-Y, Wang J, Zhang K, Luo B, Shen C (2019) Loss of mitochondrial protein CHCHD10 in skeletal muscle causes neuromuscular junction impairment. Hum Mol Genet. https://doi.org/10.1093/hmg/ddz154
26. Vandoorne T, Veys K, Guo W, Sicart A, Vints K, Swijsen A, Moisse M, Eelen G, Gounko NV, Fumagalli L, Fazal R, Germeys C, Quaegebeur A, Fendt SM, Carmeliet P, Verfaillie C, Van Damme P, Ghesquière B, De Bock K, Van Den Bosch L (2019) Differentiation but not ALS mutations in FUS rewires motor neuron metabolism. Nat Commun 10:1–12. https://doi.org/10.1038/s41467-019-12099-4
27. Uusimaa J, Kettunen J, Varilo T, Järvelä I, Kallijärvi J, Kääriäinen H, Laine M, Lapatto R, Myllynen P, Niinikoski H, Rahikkala E, Suomalainen A, Tikkanen R, Tyynismaa H, Vieira P, Zarybnicky T, Sipilä P, Kuure S, Hinttala R (2022) The Finnish genetic heritage in 2022– from diagnosis to translational research. Dis Model Mech 15:dmm049490. https://doi.org/10.1242/dmm.049490
28. Ritchie ME, Phipson B, Wu D, Hu Y, Law CW, Shi W, Smyth GK (2015) Limma powers differential expression analyses for RNA-sequencing and microarray studies. Nucleic Acids Res 43:e47–e47. https://doi.org/10.1093/nar/gkv007
29. Villanueva RAM, Chen ZJ (2019) ggplot2: elegant graphics for data analysis. Meas (Mahwah N J) 17:160–167. 2nd edn.https://doi.org/10.1080/15366367.2019.1565254
30. Frankenfield AM, Ni J, Ahmed M, Hao L (2022) Protein contaminants matter: Building universal protein contaminant libraries for DDA and DIA proteomics. J Proteome Res 21:2104–2113. https://doi.org/10.1021/acs.jproteome.2c00145
31. Martin M (2011) Cutadapt removes adapter sequences from high-throughput sequencing reads. EMBnet J 17:pp–10
32. Dobin A, Davis CA, Schlesinger F, Drenkow J, Zaleski C, Jha S, Batut P, Chaisson M, Gingeras TR (2013) STAR: ultrafast universal RNA-seq aligner. Bioinformatics 29:15–21
33. Liao Y, Smyth GK, Shi W (2019) The R package Rsubread is easier, faster, cheaper and better for alignment and quantification of RNA sequencing reads. Nucleic Acids Res 47:e47–e47. https://doi.org/10.1093/nar/gkz114
34. Love MI, Huber W, Anders S (2014) Moderated Estimation of fold change and dispersion for RNA-seq data with DESeq2. Genome Biol 15:550. https://doi.org/10.1186/s13059-014-0550-8
35. Richter U, Lahtinen T, Marttinen P, Myöhänen M, Greco D, Cannino G, Jacobs HT, Lietzén N, Nyman TA, Battersby BJ (2013) A mitochondrial ribosomal and RNA decay pathway blocks cell proliferation. Curr Biol 23:535–541. https://doi.org/10.1016/j.cub.2013.02.019
36. Straub IR, Weraarpachai W, Shoubridge EA (2021) Multi-OMICS study of a CHCHD10 variant causing ALS demonstrates metabolic rewiring and activation of Endoplasmic reticulum and mitochondrial unfolded protein responses. Hum Mol Genet 30:687–705. https://doi.org/10.1093/hmg/ddab078
37. Rabouw HH, Langereis MA, Anand AA, Visser LJ, De Groot RJ, Walter P, Van Kuppeveld FJM (2019) Small molecule ISRIB suppresses the integrated stress response within a defined window of activation. Proc Natl Acad Sci U S A 116:2097–2102. https://doi.org/10.1073/PNAS.1815767116/SUPPL_FILE/PNAS.1815767116.SAPP.PDF
38. Sturm G, Karan KR, Monzel AS, Santhanam B, Taivassalo T, Bris C, Ware SA, Cross M, Towheed A, Higgins-Chen A, McManus MJ, Cardenas A, Lin J, Epel ES, Rahman S, Vissing J, Grassi B, Levine M, Horvath S, Haller RG, Lenaers G, Wallace DC, St-Onge M-P, Tavazoie S, Procaccio V, Kaufman BA, Seifert EL, Hirano M, Picard M (2023) OxPhos defects cause hypermetabolism and reduce lifespan in cells and in patients with mitochondrial diseases. Commun Biol 6:22. https://doi.org/10.1038/s42003-022-04303-x
39. Kenvin S, Torregrosa-Muñumer R, Reidelbach M, Pennonen J, Turkia JJ, Rannila E, Kvist J, Sainio MT, Huber N, Herukka S-K, Haapasalo A, Auranen M, Trokovic R, Sharma V, Ylikallio E, Tyynismaa H (2022) Threshold of heteroplasmic truncating MT-ATP6 mutation in reprogramming, Notch hyperactivation and motor neuron metabolism. Hum Mol Genet 31:958–974. https://doi.org/10.1093/hmg/ddab299
40. Sainio MT, Rasila T, Molchanova SM, Järvilehto J, Torregrosa-Muñumer R, Harjuhaahto S, Pennonen J, Huber N, Herukka S-K, Haapasalo A, Zetterberg H, Taira T, Palmio J, Ylikallio E, Tyynismaa H, Synaptic activity and organelle trafficking in cultured human motor neurons (2022) Neurofilament light regulates axon caliber. Front Cell Dev Biol 0:3938. https://doi.org/10.3389/FCELL.2021.820105
41. Gaetani L, Blennow K, Calabresi P, Filippo M, Di, Parnetti L, Zetterberg H (2019) Neurofilament light chain as a biomarker in neurological disorders. J Neurol Neurosurg Psychiatry 90:870–881. https://doi.org/10.1136/jnnp-2018-320106
42. Genin EC, Bannwarth S, Lespinasse F, Ortega-Vila B, Fragaki K, Itoh K, Villa E, Lacas-Gervais S, Jokela M, Auranen M, Ylikallio E, Mauri-Crouzet A, Tyynismaa H, Vihola A, Augé G, Cochaud C, Sesaki H, Ricci J-E, Udd B, Vives-Bauza C, Paquis-Flucklinger V (2018) Loss of MICOS complex integrity and mitochondrial damage, but not TDP-43 mitochondrial localisation, are likely associated with severity of CHCHD10-related diseases. Neurobiol Dis 119:159–171. https://doi.org/10.1016/J.NBD.2018.07.027
43. Angelastro JM, Ignatova TN, Kukekov VG, Steindler DA, Stengren GB, Mendelsohn C, Greene LA (2003) Regulated expression of ATF5 is required for the progression of neural progenitor cells to neurons. J Neurosci 23:4590–4600. https://doi.org/10.1523/JNEUROSCI.23-11-04590.2003
44. Park Y-E, Jin-Hong S, Dae-Seong K (2020) Muscle pathology in neuromuscular disorders. Annals Clin Neurophysiol 22:51–60. https://doi.org/10.14253/kjcn.2020.22.2.51

45. Guyenet SJ, Furrer SA, Damian VM, Baughan TD, La Spada AR, Garden GA (2010) A simple composite phenotype scoring system for evaluating mouse models of cerebellar ataxia. J Vis Exp Doi. https://doi.org/10.3791/1787
46. Lin H-P, Petersen JD, Gilsrud AJ, Madruga A, D'Silva TM, Huang X, Shammas MK, Randolph NP, Li Y, Jones DR, Pacold ME, Narendra DP (2024) DELE1 promotes translation-associated homeostasis, growth, and survival in mitochondrial myopathy. BioRxiv 2024.02.29.582673. https://doi.org/10.1101/2024.02.29.582673
47. Gladyck S, Aras S, Hüttemann M, Grossman LI (2021) Regulation of COX assembly and function by twin CX9C Proteins—Implications for human disease. Cells 10. https://doi.org/10.3390/cells10020197
48. Lehmer C, Schludi MH, Ransom L, Greiling J, Junghänel M, Exner N, Riemenschneider H, Zee J, Van Broeckhoven C, Weydt P, Heneka MT, Edbauer D (2018) A novel CHCHD10 mutation implicates a Mia40-dependent mitochondrial import deficit in ALS. EMBO Mol Med 10. https://doi.org/10.15252/emmm.201708558
49. Martherus RSRM, Sluiter W, Timmer EDJ, VanHerle SJV, Smeets HJM, Ayoubi TAY (2010) Functional annotation of heart enriched mitochondrial genes GBAS and CHCHD10 through guilt by association. Biochem Biophys Res Commun 402:203–208. https://doi.org/10.1016/j.bbrc.2010.09.109
50. Purandare N, Somayajulu M, Hüttemann M, Grossman LI, Aras S (2018) The cellular stress proteins CHCHD10 and MNRR1 (CHCHD2): partners in mitochondrial and nuclear function and dysfunction. J Biol Chem 293:6517–6529. https://doi.org/10.1074/jbc.RA117.001073
51. Burstein SR, Valsecchi F, Kawamata H, Bourens M, Zeng R, Zuberi A, Milner TA, Cloonan SM, Lutz C, Barrientos A, Manfredi G (2018) In vitro and in vivo studies of the ALS-FTLD protein CHCHD10 reveal novel mitochondrial topology and protein interactions. Hum Mol Genet 27:160–177. https://doi.org/10.1093/hmg/ddx397
52. Floyd BJ, Wilkerson EM, Veling MT, Minogue CE, Xia C, Beebe ET, Wrobel RL, Cho H, Kremer LS, Alston CL, Gromek KA, Dolan BK, Ulbrich A, Stefely JA, Bohl SL, Werner KM, Jochem A, Westphall MS, Rensvold JW, Taylor RW, Prokisch H, Kim J-JP, Coon JJ, Pagliarini DJ (2016) Mitochondrial protein interaction mapping identifies regulators of respiratory chain function. Mol Cell 63:621–632. https://doi.org/10.1016/j.molcel.2016.06.033
53. Schlattner U, Tokarska-Schlattner M, Wallimann T (2006) Mitochondrial creatine kinase in human health and disease. Biochim Biophys Acta 1762:164–180. https://doi.org/10.1016/j.bbadis.2005.09.004
54. Kazak L, Cohen P (2020) Creatine metabolism: energy homeostasis, immunity and cancer biology. Nat Rev Endocrinol 16:421–436. https://doi.org/10.1038/s41574-020-0365-5
55. Giusti L, Molinaro A, Alessandrì MG, Boldrini C, Ciregia F, Lacerenza S, Ronci M, Urbani A, Cioni G, Mazzoni MR, Pizzorusso T, Lucacchini A, Baroncelli L (2019) Brain mitochondrial proteome alteration driven by creatine deficiency suggests novel therapeutic venues for creatine deficiency syndromes. Neuroscience 409:276–289. https://doi.org/10.1016/j.neuroscience.2019.03.030
56. Kostadinova I, Kondeva-Burdina M, Marinov L, Vezenkov LL, Simeonova R (2023) Newly synthesized creatine derivatives as potential neuroprotective and antioxidant agents on in vitro models of Parkinson's disease. Life (Basel) 13. https://doi.org/10.3390/life13010139
57. Smith AN, Morris JK, Carbuhn AF, Herda TJ, Keller JE, Sullivan DK, Taylor MK (2023) Creatine as a therapeutic target in Alzheimer's disease. Curr Dev Nutr 7:102011. https://doi.org/10.1016/j.cdnut.2023.102011
58. Bian X, Zhu J, Jia X, Liang W, Yu S, Li Z, Zhang W, Rao Y (2023) Suggestion of creatine as a new neurotransmitter by approaches ranging from chemical analysis and biochemistry to electrophysiology. Elife 12:RP89317. https://doi.org/10.7554/eLife.89317
59. Légaré VP, Rampal CJ, Aaltonen MJ, Janer A, Zinman L, Shoubridge EA, Armstrong GAB (2022) Loss of mitochondrial Chchd10 or Chchd2 in zebrafish leads to an ALS-like phenotype and complex I deficiency independent of the mt-ISR. BioRxiv 2022.05.02.488746. https://doi.org/10.1101/2022.05.02.488746

Publisher's note